4 4 3 3

AN INVESTIGATION OF THE NANOGRANULAR Au FILMS ELECTROLESSLY DEPOSITED ON Si SURFACES

A THESIS SUBMITTED IN PARTIAL FULFILLMENT FOR THE
DEGREE OF
MASTER OF SCIENCE
AS A PART OF THE INTEGARTED Ph.D PROGRAMME

BY

BHUVANA

CHEMISTRY AND PHYSICS OF MATERIALS UNIT
JAWAHARLAL NEHRU CENTRE FOR ADVANCED SCIENTIFIC
RESEARCH
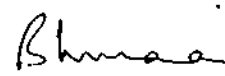BANGALORE – 560056

APRIL 2006

Declaration

I hereby declare that this thesis entitled **"An investigation of the nanogranular Au films electrolessly deposited on Si surfaces"** is an authentic record of research work carried out by me under the supervision of Prof. G. U. Kulkarni at the Chemistry and Physics of Materials Unit, Jawaharlal Nehru Centre for Advanced Scientific Research, Bangalore, India.

In keeping with the general practice of reporting scientific observations, due acknowledgement has been made whenever the work described here has been based on the findings of other investigators. Any oversight due to error of judgement is regretted.

Date: 10. 4. 06   Bhuvana

Bangalore

Certificate

Certified that the work described in this thesis titled "**An investigation of the nanogranular Au films electrolessly deposited on Si surfaces**" has been carried out by Ms. Bhuvana at the Chemistry and Physics of Materials Unit, Jawaharlal Nehru Centre for Advanced Scientific Research, Bangalore, India under my supervision and that it has not been submitted elsewhere for the award of any degree or diploma.

Date: 10 April 2006

Bangalore

Prof. G. U. Kulkarni

(Research Supervisor)

Table of Contents

Acknowledgements

Synopsis

The thesis titled 'An investigation of the nanogranular Au films electrolessly deposited on Si surfaces' presents the efforts made to exploit the method of electroless deposition in nanostructuring gold. Chapter 1 contains a brief overview on the methods employed for nanocrystalline metal films with special emphasis on the electroless process.

A systematic study carried out to obtain epitaxial Au films on Si(111) surfaces has been discussed in Chapter 2. It explains the effect of variation in plating conditions such as concentration of the plating solution, deposition time and bath temperature, on the crystallographic orientation and morphology of the deposited films.

Chapter 3 describes the formation of discrete nanostructures of Au by controlling the metal growth using surfactant molecules or by masking selected regions of the Si substrate. The effect of surfactants such as poly(vinylpyrrolidone) and mercaptoundecanoic acid as additives in the plating solution, has been studied. Alternatively, self assembling molecules such as silanes have been used as masking agents to form discrete nanostructures of Au.

Chapter 4 deals with electroless deposition of Au on Si substrates precoated with carbon. The morphology of the nanogranular film has been investigated as a function of the underlying carbon layer thickness. The chemical nature of the Au deposits inside the carbon pores is also examined. This

chapter also describes the utility of the prepared nanogranular films as substrates for Surface Enhanced Raman Scattering (SERS) from organic as well as biomolecules.

Chapter 1

An overview of nanogranular metal films

1.1 Introduction

Nanometre-sized materials have attracted a great deal of attention, in the recent years, due to the immense opportunities they offer in basic understanding as well as in a wide variety of applications. There have been continued efforts to synthesize well defined nanomaterials such as clusters, nanocrystals, nanotubes, nanowires and thin films (see Figure 1.1) [1,2]. Initial effort toward this goal started with Michael Faraday in the 19th century, who prepared Au nanoparticles in the form of a colloidal sol and termed them as 'divided metals' [3]. Of late, it has been possible to produce clusters of a given nuclearity (such as C_{60}, Au_{55}, etc.), nanocrystals of metals and semiconductors of a given size distribution, carbon and inorganic nanotubes as well as nanocrystalline thin films of various materials. The surfaces of these nanomaterials can be functionalized with different organic and biomolecules to aid desired organization at a mesoscalar level.
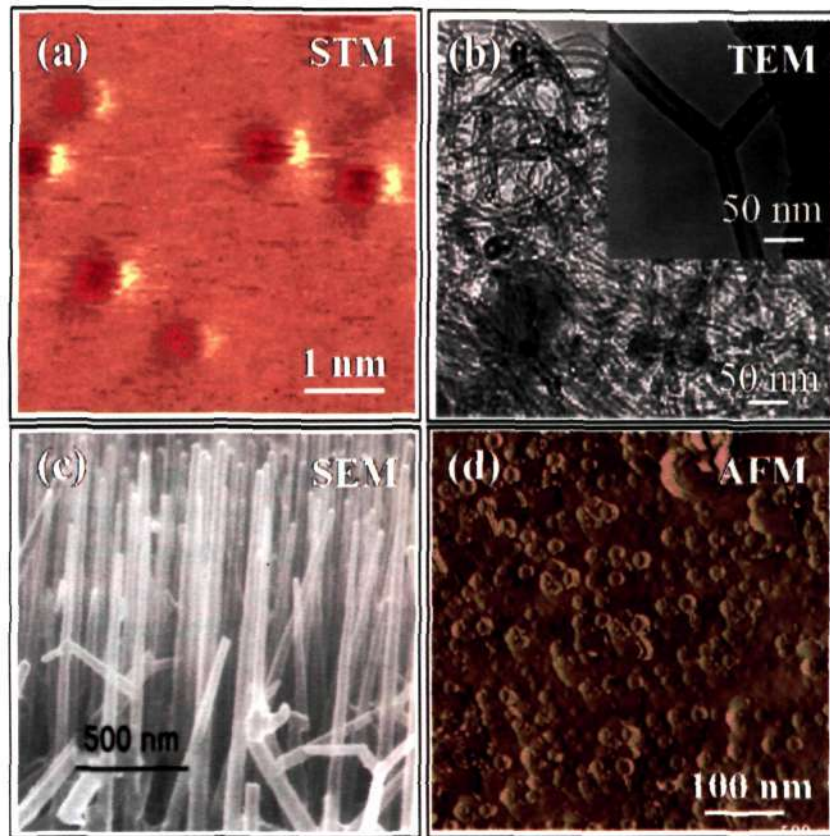
Figure 1.1 Various nanosystems, (a) Pd_{561} clusters, (b) Single-walled carbon nanotubes, inset showing a Y-junction (c) Ge nanowires and (d) a Au film.

Another aspect of the study of nanomaterials is their size dependent behaviour. The property of a nanoscale object can be quite different from that of its bulk. The difference arises due to large surface to volume ratio which contains more atoms to the surface. The change in the property is also brought about due to quantum confinement of the conduction electrons at the nanoscale. This is schematically represented in Figure 1.2. The properties of a nanosystem can also be modified by changing its shape.

Very small nanoparticles or clusters (zero dimensional) behave like atoms with discrete energy levels. Two dimensional nanomaterials
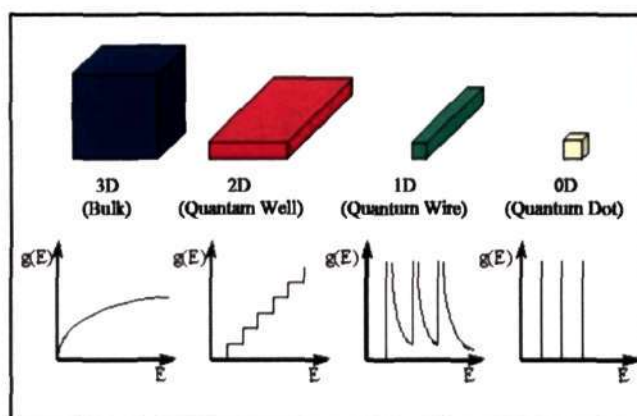
Figure 1.2 Density of states of a metallic system under quantum confinement in different dimensions.
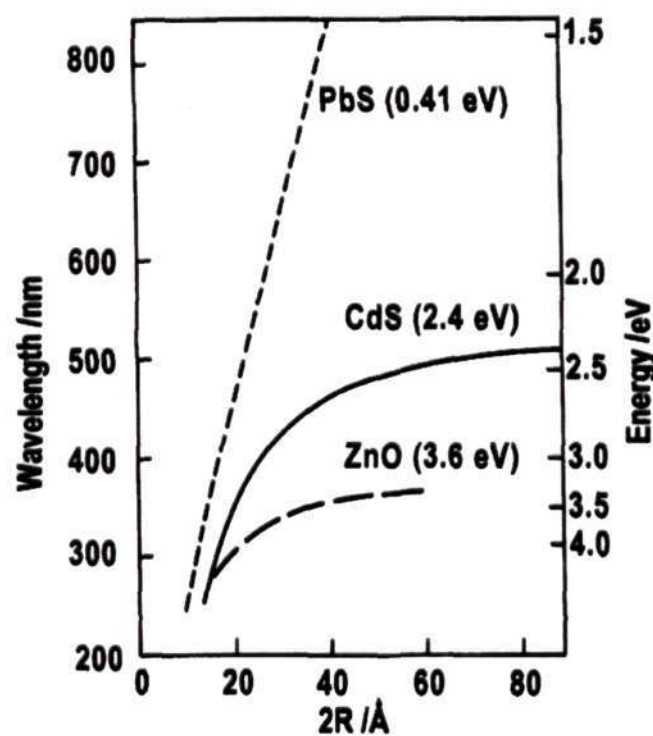
Figure 1.3 Variation of bandgap of semiconductor nanoparticles as a function of their diameter. The corresponding bulk energy gap is given in parenthesis.

such as thin films exhibit steps in their electronic density of states (DOS), while van Hove singularities (sharp spikes) are observed in the case of one dimensional analogues. It is generally accepted that the quantum confinement of electrons by the potential wells of nanometer

sized structures may provide a powerful means to control electrical, optical, magnetic and thermoelectric properties of a solid state functional material [4]. The ability to tune the properties by controlling the size and shape makes them attractive candidates for potential applications in various fields. Of particular interest are the nanocrystalline films which are notionally a blend of zero and two dimensionalities. In the following section, a brief overview of the techniques employed for nanocrystalline metal films is given with special emphasis on electroless deposition.

1.2 Nanocrystalline metal films

1.2.1 Physical methods

Among the physical methods, physical vapor deposition by resistive heating, inert gas condensation, ion sputtering, nebulised spray pyrolysis, laser ablation and laser pyrolysis are well known for producing nanocrystalline (also called nanogranular) metal films (Figure 1.4). For example, Aruna et al. have synthesized Gd nanocrystalline films using inert gas condensation technique and studied the hydrogen uptake [5]. Nanogranular Fe films (~20 nm) have been grown by dc magnetron sputtering using Si(100) wafers as substrates [6]. In another study, carbon films embedded with Fe nanoparticles have been obtained by co-deposition using ion beam sputtering [7]. Starting with metal precursors, nanocrystalline metal films have been obtained using nebulized spray pyrolysis [8]. Laser induced pyrolysis has also been employed to prepare metal films. Watanabe et al. prepared Ge-Si alloy films on Si using an

organometallic precursor [9]. Pulse laser ablation has been employed in the preparation of a wide variety of metal films. Galde et al. used this method in the case of rare-earth metals [10]. The nature of the deposited films in these cases, crucially depends on the substrate temperature among other parameters.
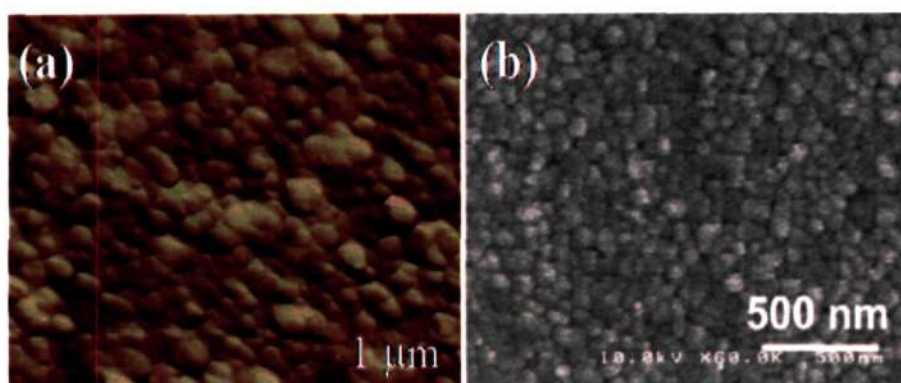
Figure 1.4   Nanocrystalline films obtained from (a) ion sputtering of Au metal (Nanolab, JNCASR) and (b) Pulsed laser deposition of Si-Ge alloy [9].

1.2.2   Chemical methods

Chemical methods of preparing nanocrystalline metal films have become popular due to their simplicity and low cost. Drop coating or spin coating of metal colloids has been used extensively. Monodispersed nanocrystals of Au, Pt, Pd, Ag, Co, etc. (protected by ligating molecules) from organo- or hydrosols form nanocrystalline films over extended regions upon slow evaporation of the solvent. An array of nanocrystals as an example is shown in Figure 1.5 [11]. The interparticle spacing in such a film can be controlled by varying the length of the ligating molecule. Spin coating of the sols has been employed to obtain nanocrystalline

metal films of desired thicknesses. O'Shrea et al. employed the above technique to synthesize a film with foam-like properties [12].

Figure 1.5 Two-dimensional arrays of thiol-derivatised Pd clusters of definite nuclearity. A two-dimensional array of thiol-derivatized Pd-Ni core-shell nanocrystals [11].

Liquid-liquid interface has been developed as a single step procedure to synthesize metal nanocrystals of desired size and to cast them in the form of a free standing nanocrystalline film [13]. In this method, an organometallic precursor such as $Au(PPh_3)Cl$ is dissolved in the organic layer (toluene or benzene) held atop an aqueous layer containing a reducing agent, like partially hydrolysed tetrakis-hydroxymethyl phosphonium chloride (THPC). In this way, the reagents are allowed to react in an extremely constricted region of the organo-aqueous interface. The novelty of this procedure is that free standing metal as well as alloy films can be prepared with a good control on the nanocrystal size. From Figure 1.6, we see that the nanocrystal diameter varies from ~8 to ~30 nm as the temperature of the reaction vessel is increased from 30 °C (room
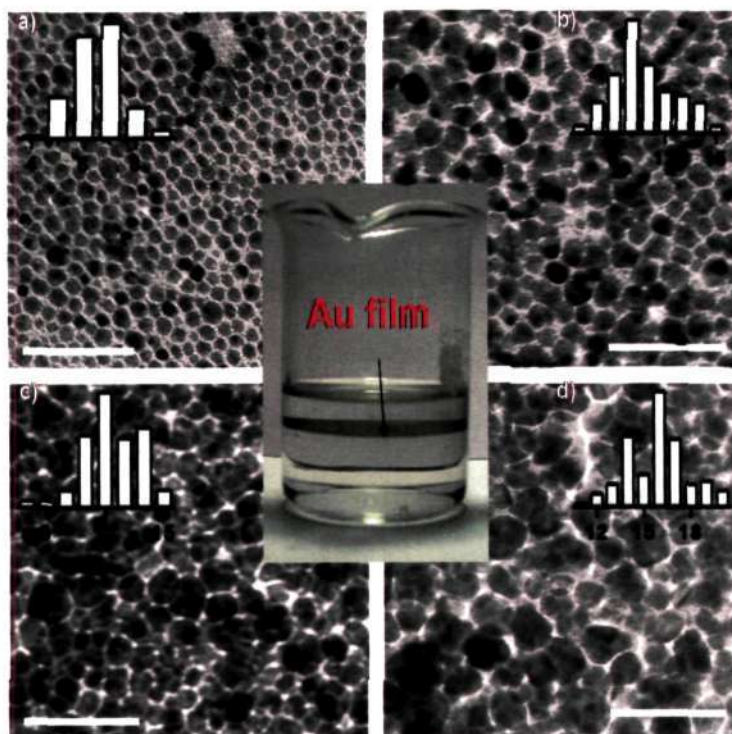
Figure 1.6   TEM images of Au nanocrystals obtained from a liquid-liquid interface at different temperatures (a) 30 (b) 45 (c) 60 and (d) 75 ^{o}C. Insets showing the size distributions of the particles in each case. At the centre, a photograph of the Au film formed at the toluene-water interface is shown [13].

temperature) to 75 ^{o}C. Accordingly, the films exhibited a variation in electrical transport properties.

In electrochemical deposition, metals and alloys from a cathode plate are deposited on to an anodic substrate by applying an external potential (Figure 1.7).   Electrodeposition has proven to be a simple method of producing nanostructured metals [14].   The theory of metal-on-metal deposition is well established [15].   The nature of the deposit can be modified easily during the electrochemical process. Important processing parameters include bath composition, pH, temperature, over potential, bath additives, etc.   To this date, a large number of systems (pure

metals, alloys, composites, and ceramics) have been electrodeposited with average grain sizes less than 100 nm. Various metals have been deposited by this method [15-18]. Figure 1.7 shows a typical example of electrochemical deposition process. O'Keeffe et al.[19] and Attenborough et al.[20] have studied the deposition of magnetic layers of Co-Ni-Cu on Cu surfaces. There are reports on electrochemical deposition of metals on highly oriented pyrolytic graphite (HOPG) surface as well. Hwang et al. have reported the deposition of Au on HOPG surface [21]. Furthermore, they have studied the deposition of Au on to a polypyrrole film deposited on HOPG [22].

$$2\,Cl^-(l) \longrightarrow Cl_2(g) + 2\,e^- \qquad 2\,Na^+(l) + 2\,e^- \longrightarrow 2\,Na(l)$$
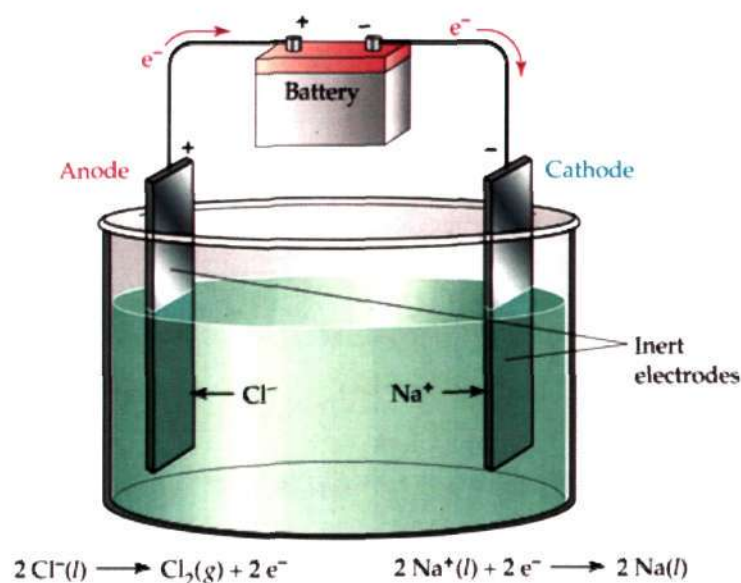
Figure 1.7   A typical electrochemical cell.

Electrochemical deposition involving semiconductor substrates have attracted much attention due to device application in electronics [23]. Figure 1.8 illustrates a possible mechanism for the deposition of metals onto a n-type semiconductor. Figure 1.8a shows a metal/metal ion redox

couple with a sufficiently negative equilibrium potential (e.g. transition metal) so that the acceptor levels have a large overlap with the conduction band edge. If the surface electron concentration in the conduction band is sufficiently high, the electrons can be transferred to the metal ion in solution, resulting in deposition of the metal. In Figure 1.8b, electrons are transferred to the metal ion from the surface states in the band gap of the semiconductor. Figure 1.8c shows the situation for a metal/metal ion coupled with a positive equilibrium potential (e.g. noble metals), in which the acceptor states overlap with the valence band of the semiconductor. In this case, holes can be ejected directly into the valence band, resulting in deposition of the metal.
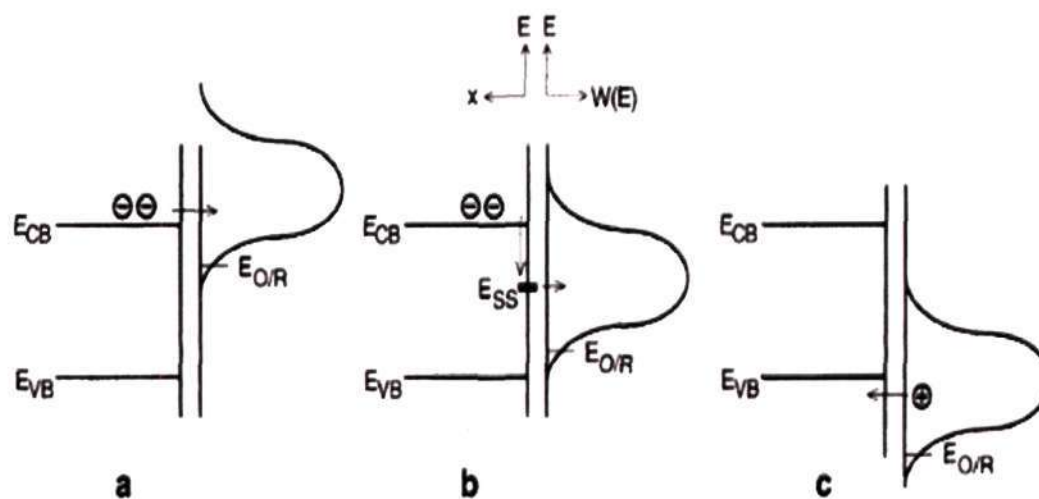
Figure 1.8 Energy band diagrams illustrating possible mechanisms of deposition of a metal onto an n-type semiconductor. (a) Transfer of electrons from the conduction band to a metal/metal ion couple with a sufficiently negative equilibrium potential, (b) transfer of electrons from surface states and (c) injection of holes into the valence band from a metal/metal ion couple with a sufficiently positive equilibrium potential [15].

The deposition of Cu, Pb, Au, Co and Ni on Si(100) or Si(111) has been well studied [15,24]. A study on the deposition of Au on H:Si(111) surface carried out by Munford et al. showed that gold nucleates exclusively along the steps and the density of nuclei is controlled by the electrode potential [17]. Ronkel et al. studied the deposition of Fe on porous silicon [25]. Interestingly, metals can also be deposited onto a semiconductor surface without applying an external bias, in a process called electroless deposition.

1.3   Electroless Deposition

Electroless deposition of metals on semiconductor surfaces involves reduction of metallic ions from a solution at the surface in the absence of an external electrical current source. It is based on an autocatalytic redox process, in which the cation of the metal to be deposited is reduced by a soluble reductant at the surface of the metal features being formed, or at the surface of catalyst used to initiate the deposition. This deposition requires the immersion of a catalytically activated surface in a plating bath containing complexed metal ions and a reducing agent. This bath needs a careful control with respect to its composition, temperature and pH. As etching is vital for Si substrates (to remove native oxide), the deposition of metals on Si is generally done from a fluoride-based solution. The half-cell reactions on Si substrate are as follows:

Anodic: $Si + 6HF \longrightarrow SiF_6^{2-} + 6H^+ + 4e^-$

Cathodic: $M^{n+} + ne^- \longrightarrow M$ (M = metal)
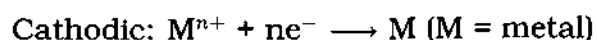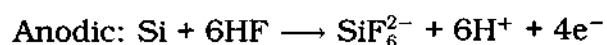
The advantages of electroless deposition are many- it is simple, relatively inexpensive, highly selective, low operating temperature and does not generally depend on the shape, size or conductivity of the substrate but yields high purity films and can be used for large-scale production. Using electroless deposition, several metals have been deposited on Si and Ge surfaces that include Cu [26-32], Al [32], Sn [32], Ni [33-35], Pd [32,36], Pt [36-39], Ag [40,41] and Au [42-45]. Magagnin et al. reported improved adhesion of Cu films on Si substrates when sodium sulfate or ascorbic acid is added to the plating solution [27]. They also examined the films by microindentation [28]. Homma et al. have monitored using STM, the nucleation and growth of Cu on Si(111). They observed that copper nucleates preferentially along step edges and appears to inhibit the step-flow etching of silicon [29]. Mechanism of Cu ion reduction on Si in dilute HF solution has been discussed by Norga et al. [30]. Gorostiza et al. studied the electroless deposition of Ni on Si substrates by varying the pH of the plating solution [34]. At pH of 1.2, no deposition was seen while at pH of 8.0, the Ni deposition was found to be rich. Furukawa et al. have shown that optimal conditions of temperature and pH are necessary to obtain smooth Ni films [35]. Ni films can be deposited directly onto Si without activation, although pre-roughening of the surface has been found to be essential to obtain good adhesion. The effect of HF concentration on the initial stages of the electroless deposition of various metals on Si(100) has been carefully studied by Nagahara et al. using atomic force microscopy. The rate of metal deposition on the

nature of the dopant has also been studied [32]. The effect of Pt and Pd electroless deposition on pyrolysed photoresist films grown on Si was investigated by Liang et al.[36]. They found that the photoresist helped in accelerating the electron transfer process. Kuznetsov et al. studied the electrical properties of the structures produced by treatment of Si with HF solutions of Pt salt [37]. They found that the treatment of Si in a dilute HF solution containing sodium chloroplatinate results in spontaneous Pt deposition and the formation of the dielectric interfacial layer between the Pt and Si substrate upto hundreds of nanometers. The thickness of the dielectric interface layer increases with the time of deposition. For equal deposition times, more Pt was found to be deposited on p-Si substrates than on n-Si substrates [38]. In some cases such as Pt on p-Si(100), both metal and its silicide have been detected [39]. Recently, Kalkan and Fonash have reported Ag nanoparticle ensembles on nanostructured Si films and studied using atomic force microscopy and surface diffraction [41].

Deposition of gold films from fluoride solutions on Si and Ge surfaces has been studied by Krikshtopaitia et al. about thirty years ago [42]. Magagnin et al. deposited Au on Si and Ge surfaces and examined the orientation and chemical nature of the metal at Au-Si and Au-Ge interfaces [43]. Based on core-level spectral measurements, they reported the presence of a chemical bond at the Au-Ge interface whereas no such bonding was observed for the Au-Si interface. Warren et al. studied the formation of Au clusters on H:Si(1 1 1) surface. The AFM images in Figure

a)

800 nm x 800 nm

b)

1000 nm x 1000 nm

c)

1000 nm x 1000 nm

d)

1000 nm x 1000 nm
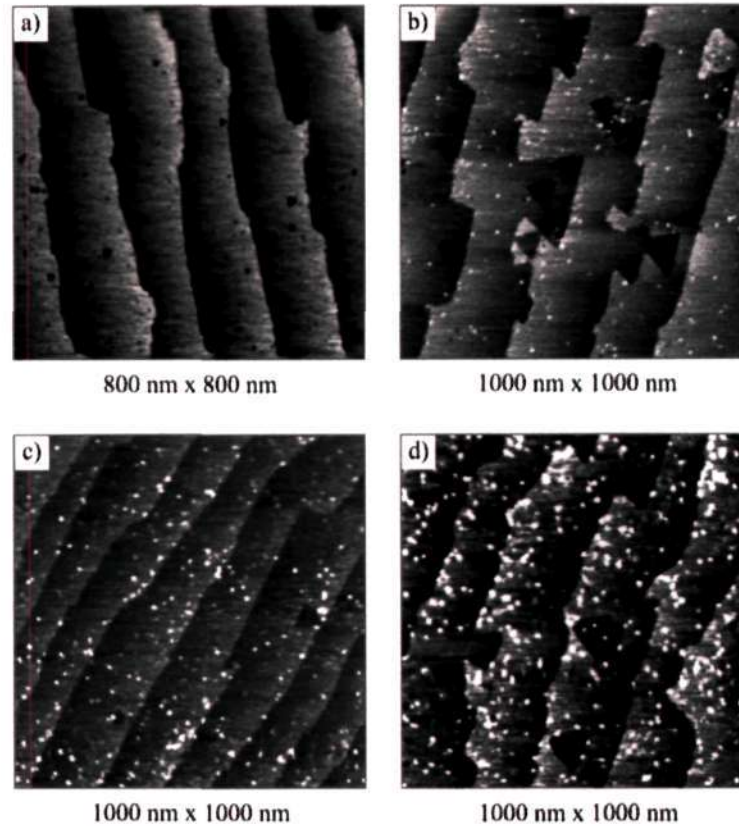
Figure 1.9   Ex-situ AFM image of the monohydride-terminated n-Si(111) surface before (a) Au deposition, (b) after 1 s, (c) 5 s and (d) 30 s of exposure to the 1 μM K[AuCl$_4$] plating solution [44].

1.9 show the different stages in the cluster formation with variation in the deposition time [44]. Based on surface X-ray diffraction measurements, the authors concluded that the Au clusters formed are epitaxially aligned with respect to the substrate. For metals with high positive equilibrium potentials such as Au, there is a strong overlap between the acceptor state in solution and the semiconductor valence band. Therefore, electroless deposition occurs via hole injection into the semiconductor valence band. As a consequence, the semiconductor is oxidised (and etched, it depends on the semiconductor) as the noble metal is deposited [15]. The net
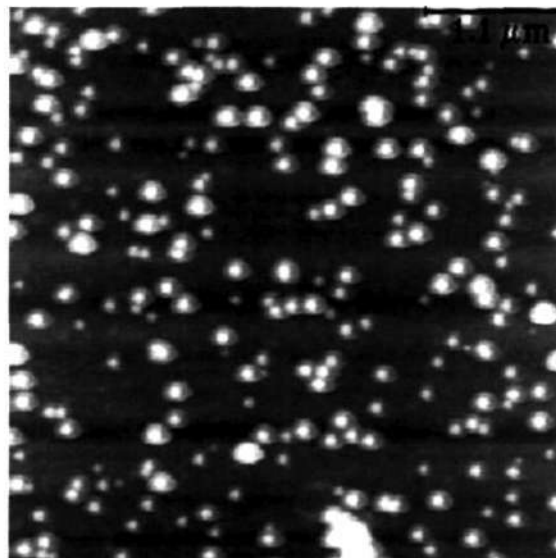
Figure 1.10   Non-contact AFM image following 610 s of Au deposition from 0.500 M HF.

process involves deposition of Au, and dissolution of Si:

$$AuCl_4^- \longrightarrow Au + 4Cl^- + 3h^+$$

$$Si + 2h^+ \longrightarrow Si^{2+}$$
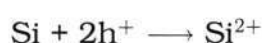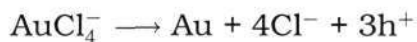
Rossiter and Suni [45] deposited Au nanoclusters from aqueous mixtures of HF and KAu(CN)$_2$ onto Si(111) (Figure 1.10). Electroless deposition of Au films onto III-V semiconductors (GaAs, InP, GaP and Al$_x$Ga$_{1-x}$As) have also been achieved on the surfaces activated with Pd nuclei [46].

1.4   Nanostructuring by Electroless Deposition

Electroless deposition of metals on semiconductor surfaces is an important process in view of its application in electronics and nanofabrication.   It is based on selective deposition and can be achieved either by the selective deactivation of a catalytic substrate or by the

selective activation of a non-reactive surface by a catalyst. Electroless deposition combined with various other techniques such as microcontact printing, templated growth and self assembly is a powerful technique for nanostructuring.

Using electroless deposition in combination with microcontact printing, various patterns have been generated. The capability of microcontact printing (μCP) to transfer chemical reagents from an elastometric stamp to a substrate is used to direct the electroless deposition. For instance, Cu has been patterned onto 15 x 15 sq-inch glass substrates by (i) self-assembly of a thin layer of amino-derivatized silanes to the glass, (ii) binding Pd/Sn catalytic particles to the silanes, (iii) electroless deposition of 120 nm of Cu on the catalytic surface, (iv) microcontact printing hexadecanethiol on the Cu film using an accurate printing tool, and finally (v) selectively etching the printed Cu using hexadecanethiol as a resist. This method is particularly attractive for the fabrication of metallic gates for thin-film transistor liquid-crystal displays [47]. Whitesides and co-workers [48] illustrated an electroless deposition catalyzed by colloids resulting in the formation of metal structures having submicron dimensions (Figure 1.11). They adopted new methods to reduce the size of the metal features made by electroless process to fabricate complex patterned surfaces [49] and the dimensions of the patterns thus obtained were compared with that obtained by e-beam lithography [50].

Anodic aluminum oxide film can be produced upon aluminum metal when aluminum is made the anode in an electrolyte, which has been
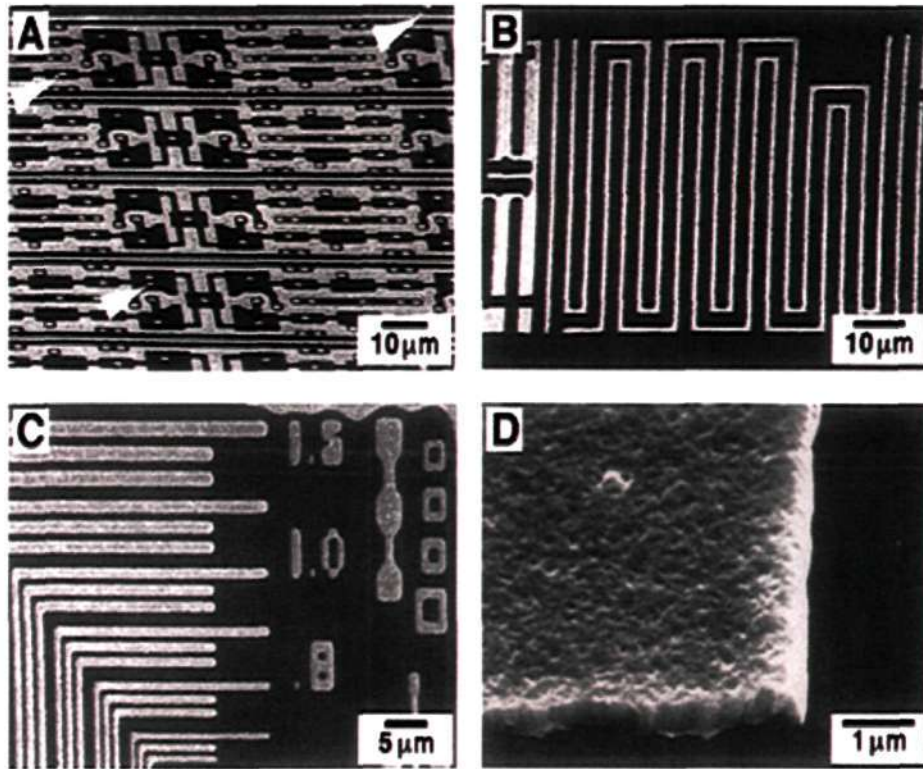
Figure 1.11   Microstructures produced by the combination of microcontact printing of colloids and electroless metallization. (A-D) SEM images of microstructures fabricated with microcontact printing of palladium colloids on (Si/SiO$_2$) (A, D), polyimide (B), and glass (C) followed by electroless deposition of copper (bright regions). (D) SEM image showing a fracture profile of a copper line [49].

studied in detail over the last five decades. Nanostructures with hollow interiors such as anodic aluminium oxide have been the focus of current research due to their potential use as templates in metal deposition. Zhang et al. [51] and Tokuda et al. [52] synthesized Ag nanotubes electrolessly using porous anodic aluminium oxide as template (Figure 1.12).

By using an ultrathin film of microphase-separated poly(styrene-block-methyl methacrylate) as a template, Zehner and Sita [53] generated
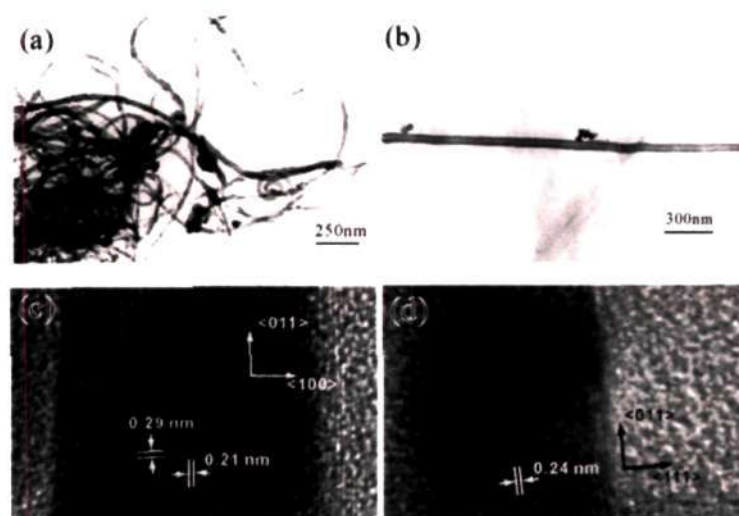
Figure 1.12 (a, b) Typical TEM images of Ag nanotubes synthesized by electroless deposition in AAO templates. (c, d) HRTEM images of the wall of silver nanotubes [51].

nanometer-scale patterns of tetraalkylammonium passivated palladium colloids. This pattern serves, in turn, as the template for the electroless deposition of 20 nm wide copper nanostructures, which is approximately a factor of two, smaller than feature sizes that can be generated by state-of-the-art lithographic processes [54].

Arrays of aligned, multiwalled carbon nanotubes were produced by catalytically pyrolyzing acetylene within the pores of an anodic aluminum oxide template. Small cobalt catalyst particles were predeposited elec-trochemically at the bottom of the pores. The nanotubes were found to be open at one end, making it possible fill the tubes with metals or other materials [55, 56]. Nickel and cobalt metals were deposited in the interior of the tubes using nanoscale electroless deposition. The deposited metals contained small quantities of phosphorus or boron, according to the reducing agent used in the electroless deposition process

(hypophosphite or dimethylamine-borane). The deposits, in general, consisted of discontinuous, polycrystalline metal filling most of the length of the nanotube, but in the case of Co reduced with hypophosphite, continuous polycrystalline deposits of up to 3 μm were observed. The Ni crystallites inside the tubes had fcc structures with cell constants of 3.56 Å, slightly larger than the 3.52 Ålattice constant of bulk nickel possibly due to the inclusion of P [55]. Ang et al. activated carbon nanotubes with Pd-Sn catalytic nuclei via a single step approach. These activated nanotubes were then used as precursors for obtaining nickel- and palladium-decorated nanotubes via electroless plating [56]. In an interesting experiment, Bittner et al. [57] demonstrated the deposited of Co, Pd/Ni in and around Tobacoo Mosaic Virus (TMV) by electroless process (Figure 1.13).

Of late, electrochemical deposition has been used in drug delivery. This method is used to create thin metallic films that contain and release a wide range of drugs over long periods in vitro. They have advantage over polymer coating technologies with respect to rate of delivery and the stability of the drugs [58].

The discussions in the above sections makes the electroless deposition method a viable technique for gold nanostructuring. In this work, a systematic study of gold deposition by electroless method using potassium salt of gold in fluoride solution has been carried out. Silicon wafers of (100) and (111) orientations were used to study the effect
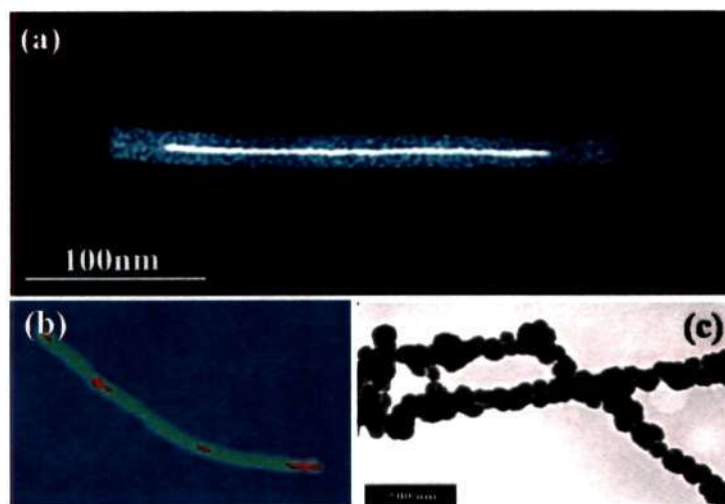
Figure 1.13 Transmission electron micrograph of a 300 nm long virus with a 150 nm long and 3 nm wide Co wire (white) in the inner channel. (b) Transmission electron micrographs of two tubular viruses (each 300 nm long) with five 3 nm Pd/Ni clusters in the inner channels. (c) Metallization of the exterior surface by Pt/Ni [57].

of crystallographic orientation of deposited films. The presence of surfactants as additives in the plating solution has also been studied. Selective deposition of Au has been carried out using silane as a masking agent to obtain various nanostructures like, island films, cellular networks and nanowires. The role of carbon overlayer on Si during electroless deposition of Au is also studied. The deposited films were used as substrates for Surface Enhanced Raman Scattering (SERS) measurements of organic and biomolecules.

Chapter 2

A systematic study of electroless deposition of Au on Si substrates

2.1 Scope of study

Gold films serve as substrates in a variety of studies. Both physical and chemical methods have been employed for preparing the films. Among chemical methods, the electroless method is simple and straightforward, and yields uniform nanogranular films [43]. Various physical parameters such as composition and concentration of the plating solution and its pH, deposition time, and bath temperature are known to be important for the epitaxial growth of the metal film during the electroless deposition process. Although there have been many studies on the deposition of Au films on Si substrates by the electroless method [42-45], there is no comprehensive report on how the various experimental parameters influence the metal deposition. We have sought to carry out a systematic investigation of the electroless deposition of Au on Si.

2.2 Introduction

Electroless deposition of Au on surfaces of Si and Ge is known since three decades. Krikshtopaitia et al. have studied the deposition of Au on Si and Ge surfaces from fluoride solutions [42]. Employing X-ray photoelectron spectroscopy (XPS), Magagnin et al. examined similarly prepared Au films on Si and Ge substrates and reported that the interaction at the Au-Ge interface was relatively stronger than at the Au-Si interface [43]. Warren et al. have studied the formation of Au deposits, epitaxially aligned with respect to the substrate, Si(111):H [44]. Using a cyanide based plating solution, Rossiter and Suni have studied the growth of the nanodeposits [45].

We considered it interesting to investigate Au nanogranular films on Si(111) and Si(100) substrates prepared by electroless deposition under different plating conditions. For this purpose, we used plating solutions containing different concentrations of the gold precursor ($KAuCl_4$) and varied the rate of deposition as a function of time and temperature. We have thus obtained a set of optimal conditions for the growth of well-oriented Au(111) films on Si(111). We have monitored the orientation of the films using X-ray diffraction (XRD) and the surface morphology by atomic force microscopy (AFM). The film thickness was measured by means of optical profilometry (OP). Furthermore, we have examined the effect of annealing at elevated temperatures on the morphology of the films.

2.3 Experimental section

2.3.1 Cleaning Si substrates

In order to obtain smooth well-oriented films, cleanliness of the surface is crucial. The following standard technique was followed for this purpose [59]. The Si(111) or Si(100) substrate was cleaned by sonicating in acetone and double distilled water, and was UV irradiated at room temperature for 15 minutes. It was cleaned further by heating at 80 °C in piranha solution (1:2 H_2O_2:H_2SO_4) *(Caution: this mixture reacts violently with organic matter)* for 10 minutes. Prior to deposition, the substrate was etched in concentrated HF for 10 minutes, rinsed with double distilled water and dried under flowing argon. This results in a H-terminated Si(111) surface with very low density of defects [60].

2.3.2 Gold deposition

In order to prepare the precursor - potassium tetrachloroaurate (KAuCl$_4$), aqueous HAuCl$_4$ and KOH solutions were mixed in 1:1 molar ratio and heated for 30 minutes. Recrystallization of the product was done from ethanol. The 'plating solution' was prepared by dissolving KAuCl$_4$ in 5 M HF. After cleaning and drying, the Si substrate was immediately used for electroless deposition of Au. The substrate was dipped in a 5 mL of the plating solution taken in a Teflon container. The depositions have been carried out at different bath temperatures for different time durations. Following the procedure, three sets of films were prepared:

(a) The $AuCl_4^-$ concentration of the plating solution was varied in the range of 0.02-5 mM keeping the deposition time as 30 minutes and the bath temperature, 28 °C.

(b) The time of deposition was varied from 5 to 150 minutes. The $AuCl_4^-$ ion concentration in the plating solution was 0.1 mM and the bath temperature, 28 °C.

(c) The film deposition was also carried out at various bath temperatures (0 to 60 °C) for 30 minutes using a plating solution of 0.1 mM $AuCl_4^-$ concentration.

Following deposition, the substrates were carefully rinsed with double distilled water and dried under flowing argon. Experimental parameters used for the sample preparation are listed in Table 2.1.

2.3.3 Characterization Techniques

The films were characterized by X-ray diffraction (XRD), atomic force microscopy (AFM) and optical profilometer (OP), the details of which are given below.

X-ray diffraction: XRD measurements were performed using Cu K_α (1.5406 Å) radiation with scan rate of 1 deg/min using a Rigaku, Miniflex diffractometer. The X-ray tube was set at 40 kV and 30 mA. With a receiving slit of 0.3 mm wide and a scintillation counter as detector, the θ-2θ scans were performed.

Atomic force microscopy: AFM measurements were made using a Digital Instruments Multimode head attached to a Nanoscope-IV con-

Table 2.1 Electroless deposition of Au films on Si(1 1 1): The plating conditions for various samples are listed. Primed numbers indicate samples with Si(100) as substrate.

Sample number	KAuCl$_4$ (mM)	Time of deposition (min)	Bath temperature (°C)
1	0.02		
2, 2'	0.1		
3	0.5	30	
4	1.0		
5	5.0		
6		5	
7		10	28
8		15	
9		20	
10		45	
11	0.1	60	
12		90	
13, 13'		120	
14		150	
15		30	0
16		30	60

troller (Veeco, USA). Standard Si$_3$N$_4$ cantilevers were used for the normal topography and friction mode imaging in the contact mode. For the tapping mode, etched silicon cantilevers were employed. The rms roughness values were obtained from the image analysis tools available with the instrument. Nanoindentation experiments were performed in the tapping mode using a cantilever carrying a pyramidal diamond tip (spring constant, 278 Nm^{-1} and resonance frequency, 52.8 Hz). The indented impression was imaged with the same tip. The hardness was calculated from the load-displacement data.

Optical profiler: To measure the film thickness, a step was created by

partially dipping the Si substrates vertically in the plating solution. The step was measured across bare Si and deposited Au film using Wyko NT1100 (Veeco, USA) optical profiler. The PSI mode was employed with a field of view (FOV) and objective lens magnification as 1X and 20X respectively.

2.4 Results and Discussion

Deposition of Au takes place due to the reduction of Au^{3+} ions on the Si surface. Half cell reactions are as follows:

Anodic: $Si + 6HF \longrightarrow SiF_6^{2-} + 6H^+ + 4e^-$

Cathodic: $Au^{3+} + 3e^- \longrightarrow Au$ (plating medium)
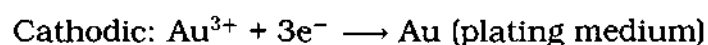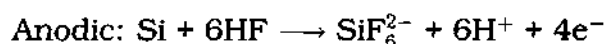
X-ray diffraction patterns of the Au films on Si(111) obtained by varying the concentration of the plating solution are shown in Figure 2.1. For small concentrations of the $AuCl_4^-$ ion, say 0.02 mM, with a deposition time of 30 minutes and bath temperature as 28 °C (**1**, see Table 2.1), we see only one peak in the diffraction pattern at 2θ of 39.20° corresponding to d-spacing of 2.295 Å, matching closely with the d_{111}-spacing of the bulk Au (2.355 Å) [44].

A similar observation has been made by Kuwahara et al. [61], who reported a difference in the d-spacing of 0.04 Åfor the epitaxial Au film on Si(111). The intensity of the (111) diffraction peak grows gradually as the concentration of $AuCl_4^-$ ion is increased from 0.02 to 1 mM (**1-4**) with no evidence of other diffraction peaks. At higher concentrations (5 mM, **5**), however, we observe additional peaks at 38.24° and 44.42° corresponding
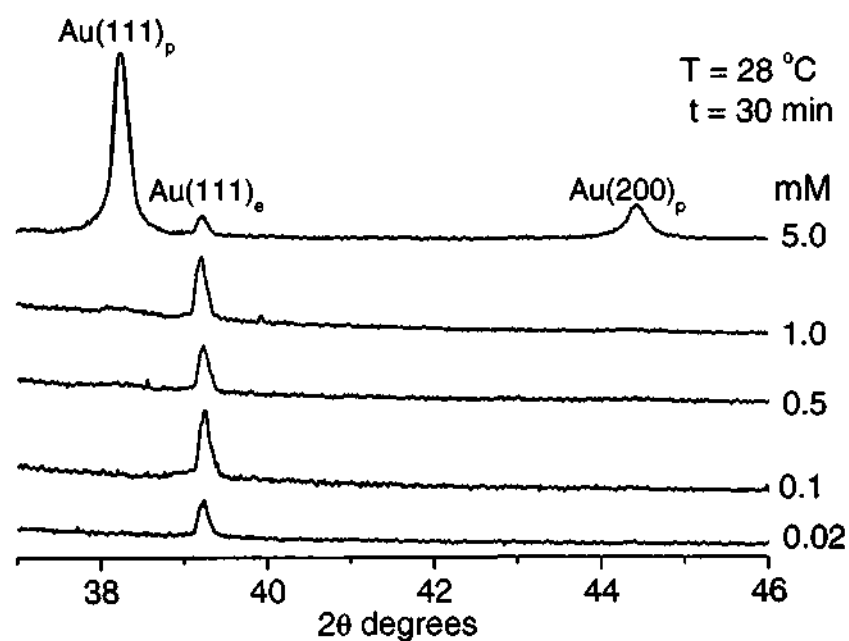
Figure 2.1   X-ray Diffraction patterns of Au films deposited on Si(111) substrates with different concentrations of the plating solution (KAuCl$_4$ in 5 M HF) at room temperature, 28 °C for 30 minutes.

to bulk Au spacings of d_{111} (2.350 Å) and d_{200} (2.039 Å) respectively. The

peak at 2.295 Å from lower epitaxial layer is much reduced in intensity.

However, the Au films grown on Si(100) substrates are polycrystalline in

nature (see Table 2.1).

The diffraction patterns obtained with varying the time of deposition

are shown in Figure 2.2. The peak at 2θ of 39.20° (d-spacing, 2.295

Å) corresponding to Au(111) plane is observed for 30 and 60 minutes.

As the deposition time is increased to 150 minutes, the peaks at 38.24°

and 44.42° corresponding to bulk Au spacings of d_{111} (2.350 Å) and d_{200}
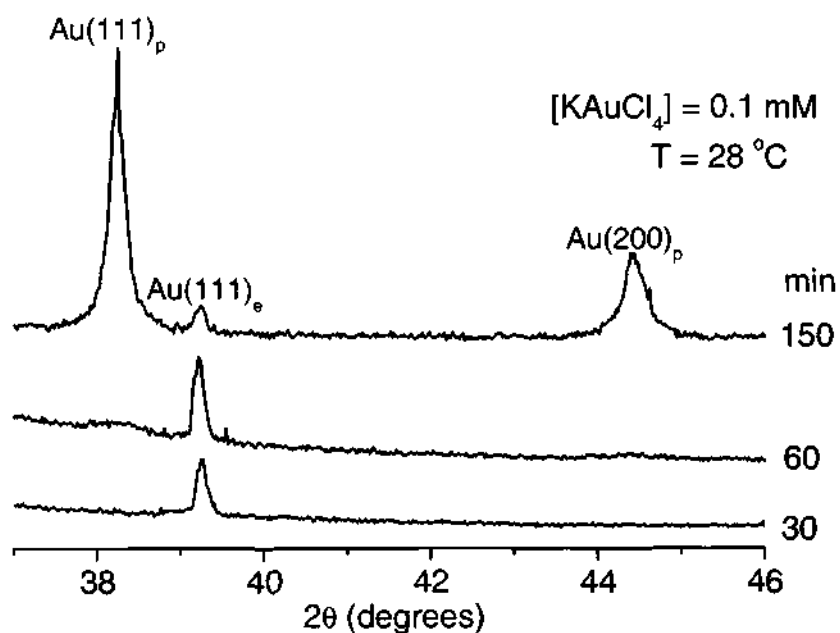
Figure 2.2   X-ray diffraction patterns of Au films deposited on Si(111) substrates for different time durations in a bath containing 0.1 mM plating solution at room temperature, 28 °C.

(2.039 Å) respectively are observed, indicating the polycrystalline nature of the film. Hence, it is important to note that the oriented Au film turns into polycrystalline if the deposition is carried out for more than 60 minutes in a 0.1 mM plating solution with the bath temperature of 28 °C. The thicknesses of the films have been measured employing optical profilometry (Figure 2.3). From the figure, we observe steps of 29, 59 and 365 nm for 30, 60 and 90 minutes of deposition(**2, 11** and **12**, see Table 2.1) respectively. Using AFM, the rms roughness values of the films are found to be 7.9, 12.8 and 17.1 nm respectively. Similar values of roughness have been obtained by Magagnin et al. [43]. Naturally, this
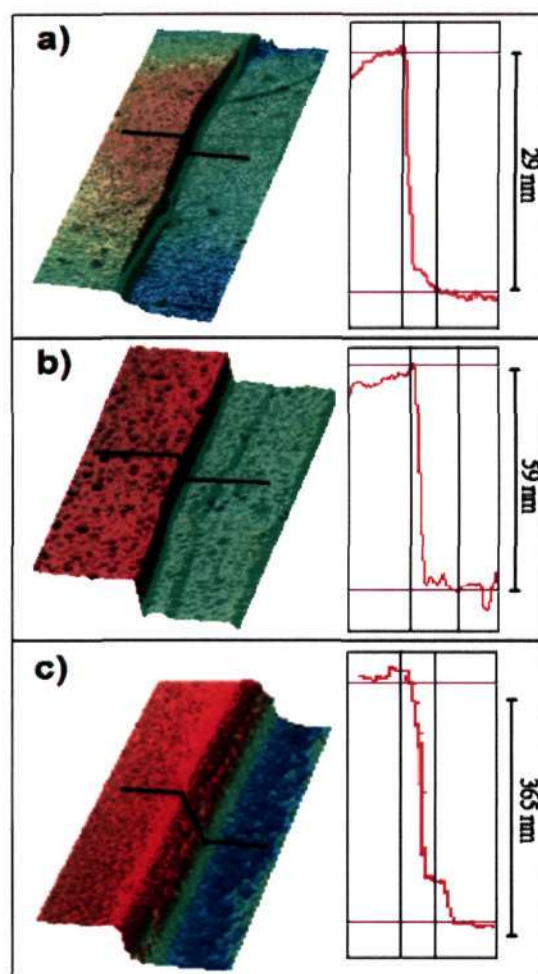
Figure 2.3 Profilometric measurements on Au films obtained by dipping Si(111) substrates in the plating solution for (a) 30 min, (b) 60 min and (c) 90 min. The deposition was carried out under the standard plating conditions (0.1 mM KAuCl$_4$, 28 °C)

sets a lower limit of thickness for an uniform Au film. In other words, the

thickness of the film deposited by this method could be controlled within

a few nanometres by varying the deposition time.

Figure 2.4 shows that the rate of deposition as measured by OP, varies

proportionally with time. During the first hour, the deposition is at the

rate of 1.03 nm/min (**2, 6-11**, see Table 2.1) and at longer durations,

there is almost an order of magnitude rise, 9.04 nm/min (**12-14**).
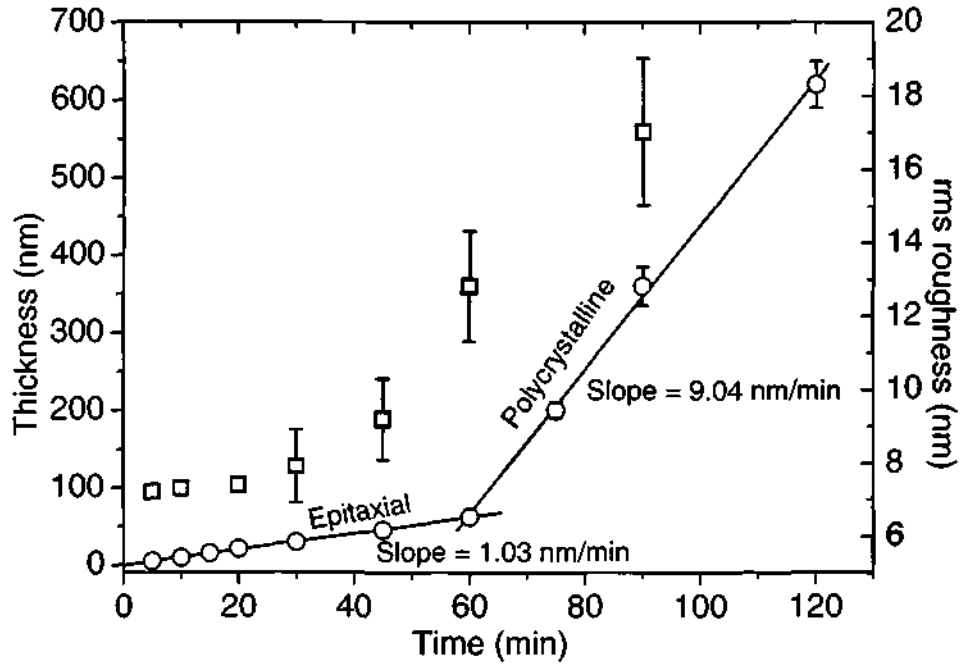
Figure 2.4   Variation in the thickness of the films (circle) as a function of deposition time in the standard plating solution. The variation in the rms roughness values (square) estimated from 2 x 2 μm^2 area using AFM, is also shown.

Referring to Figure 2.2, we notice that the change of behavior coincides with the epitaxial mode of growth becoming polycrystalline. The rms roughness values obtained from contact AFM (see Figure 2.4) also exhibit a similar trend, implying that a change in the rate of deposition owes much to the increased roughness from polycrystallinity. From the above observations, it appears that the deposition time gives a good control on the thickness of the film.

Figure 2.5 shows the diffraction patterns obtained for Au films deposited at different bath temperatures for 30 minutes in 0.1 mM plating solution.

[KAuCl$_4$] = 0.1 mM
t = 30 min
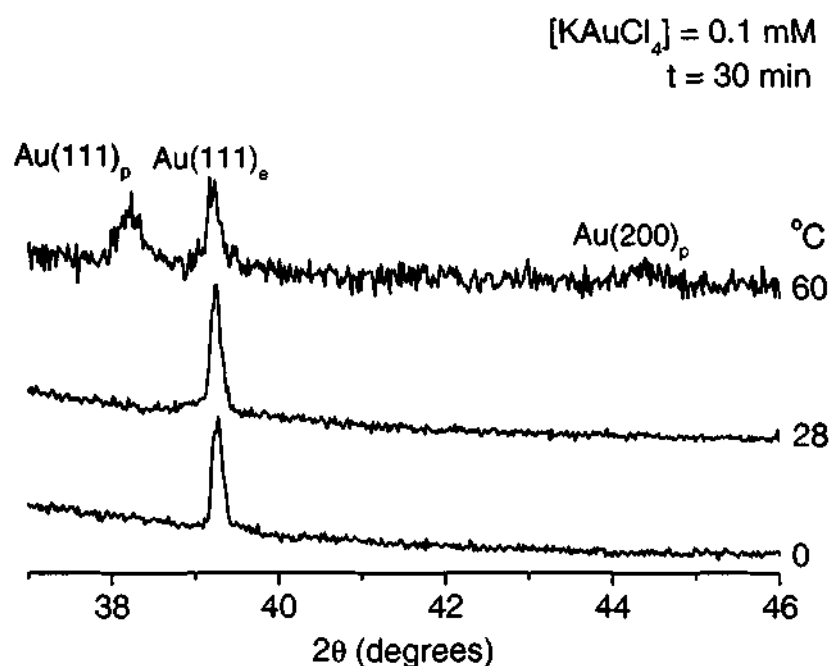
Figure 2.5 X-ray diffraction patterns of Au films deposited for 30 minutes on Si(111) substrates at different the bath temperatures containing 0.1 mM plating solution.

At 0 and 28 °C, the peak is seen at 2θ of 39.20° that corresponds to epitaxial Au(111) plane. As the temperature is increased to 60 °C, the polycrystalline peaks are appear. The lower intensity of the (111) peak implies that the epitaxial growth is somewhat inhibited at 60 °C (16).

In order to improve the texture, a film (2) was subjected to annealing at elevated temperatures of 250 and 300 °C. In Figure 2.6 AFM images and diffraction measurements after annealing at 250 °C for different time durations are shown. Figure 2.6a shows a AFM image of the as-deposited film. It is granular and the granules appear agglomerated measuring hundreds of nanometres. Annealing at 250 °C for 2 hours
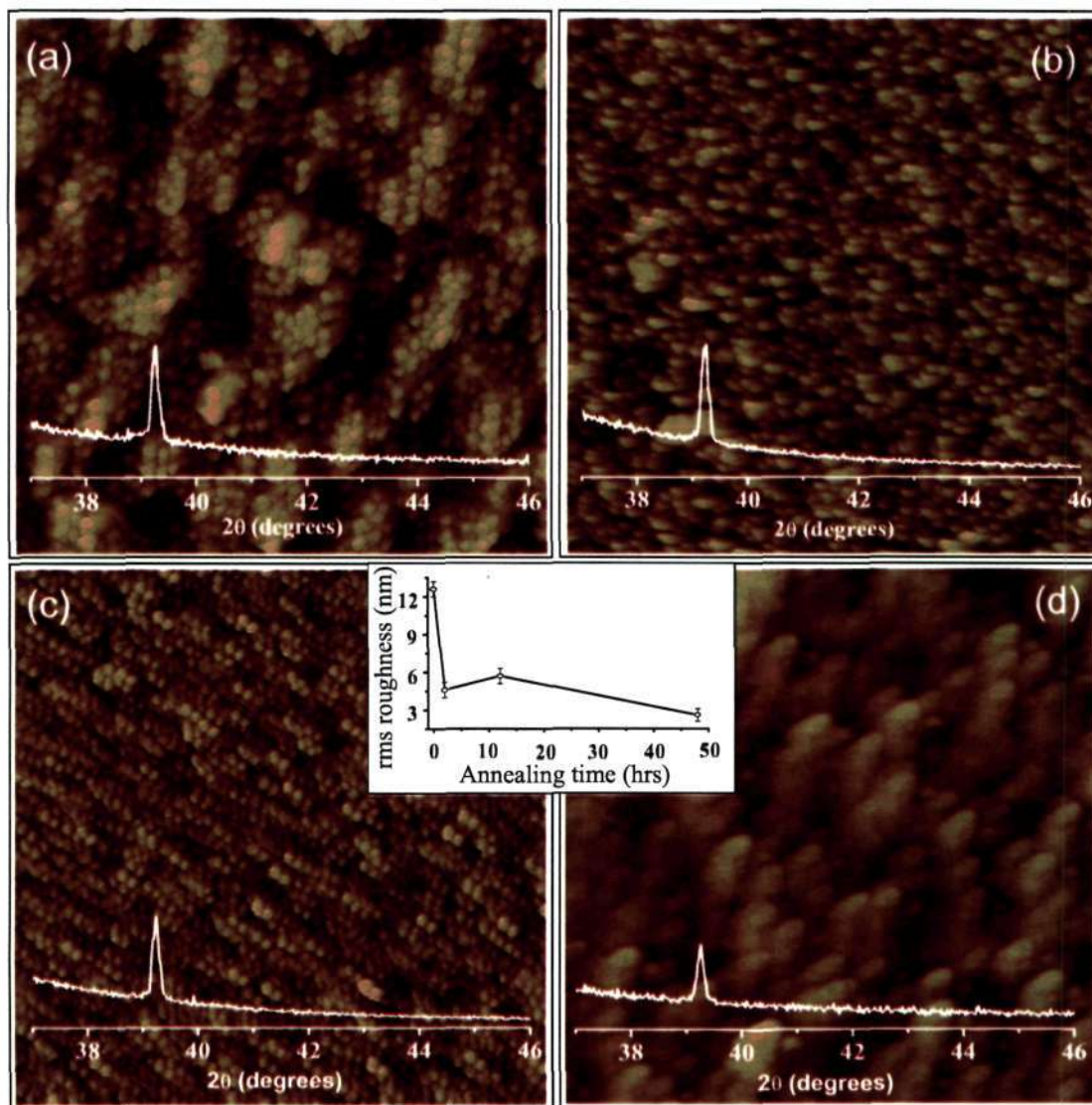
Figure 2.6 Tapping mode AFM images (2 x 2 μm^2) obtained after annealing an Au film at 250 ^{o}C for different time durations (a) as prepared (0 h), (b) 2 h, (c) 12 h and (d) 48 h. Variation in the rms roughness values estimated from AFM analysis is shown in the centre. The film was prepared under standard plating conditions (0.1 mM KAuCl$_4$, 28 ^{o}C, 30 min). In each case, the corresponding XRD patterns are shown.
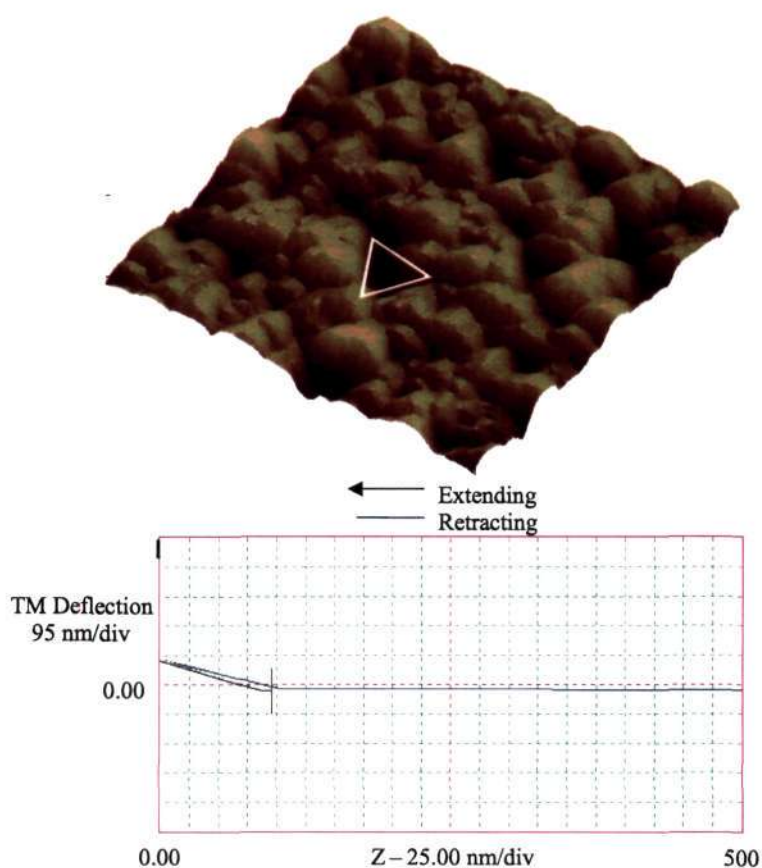
Figure 2.7 (a) Tapping mode AFM image showing the indented film (1x1 μm^2) and the triangle indicating the indented region. (b) The F-d curve obtained during the indentation.

(Figure 2.6b) improved the surface topography. With further annealing for 10 hours, the particles of size ~35 nm appear closely packed. Additional annealing, however, makes the particles grow almost three times bigger (see Figure 2.6d). The roughness values obtained from AFM analysis (see inset of Figure 2.6) show a sharp decrease from ~12 to ~5 nm following annealing. Interestingly, the (111) orientation of the film remains almost unaffected as evident from the X-ray diffraction patterns shown along with the images. Our results are comparable to the literature reports based on the deposition methods. Mancini and Rimini [62] have shown

in the case of Au films on Si deposited in vacuum, that the (111) texture improved from 60% to 90% with annealing [63]. However, we have found that annealing at even higher temperatures increases polycrystallinity (e.g. 300 °C for 1 hour).

The mechanical properties of the Au films have been measured by nanoindentation following literature procedures [64-67]. Figure 2.7 shows the AFM image of an indented region (**2**, see Table 2.1) along with the force-distance response. The projected area of the indented surface is estimated to be 8321 nm^2. The hardness was calculated using the formula, $H = F/A$, where F is the applied force and A, the projected area of indentation. The estimated hardness of the Au film was 2.19±0.1GPa. While bulk Au has much lower hardness (0.64 GPa), the obtained value may be compared with the hardness of sputtered Au films, 2.01 GPa [66].

2.5 Summary

The present study has established experimental conditions optimal for electroless deposition of Au(111) films of desired thickness. Thus, on a Si(111) substrate, a deposition carried out for 30 minutes, at room temperature with a 0.1 mM $KAuCl_4$ in 5 M HF plating solution, produces a well oriented Au film of thickness, ~29 nm. The hardness measured by nanoindentation was 2.19±0.1 GPa. Higher precursor concentrations, higher bath temperatures or longer deposition times produce polycrystalline films. For a given concentration of the precursor (0.1 mM), the film thickness is found to increase linearly with deposition

time during the first hour and the growth becomes much faster at longer durations, with the film turning to ~polycrystalline. Annealing at 250 °C for 12 hours results in a well-oriented film with reduced rms roughness. The depositions on Si(100) substrates yielded polycrystalline films.

Chapter 3

Nanostructures from electroless deposition

3.1 Scope of study

Template assisted growth of metal nanostructures by electroless deposition has been employed by a number of researchers. These methods crucially relay on the quality of the template or the mask, the preparation of which can be involved and cumbersome. To our knowledge, there has been no report of using only surfactant or self-assembling molecules while nanostructuring metals electrolessly. We have attempted to create discrete nanostructures of Au by controlling its growth using surfactant molecules or by carefully masking selected regions of the substrate (Si) by self-assembling molecules.

3.2 Introduction

Electroless deposition has been effectively employed for growing desired nanostructures such as islands, nanowires etc. on semiconductor

surfaces. Rota et al. obtained regular arrays of Au deposits along the steps of Si(111) surface [68]. Magagnin et al. produced nanoislands of Au by selective galvanic deposition using a AOT micellar plating solution [69]. Starting with aminothiolate self-assembled monolayers, Kind et al. generated Pd and Co-Pd islands by selective electroless deposition [70]. Recently, the electroless method is used to produce submicron to nanometric metal structures. Guan et al. patterned Au microstructures on glass and Si substrates using a combination of microcontact printing and electroless plating [71]. Using a stamp coated with Pd(II) catalytic precursor, directed deposition of Cu has been achieved [72]. Whitesides and coworkers have obtained desired patterns of electrolessly deposited metals by a selective etching process [48,50,73].

Template assisted electroless deposition of metals is also well known. Martin and coworkers used polycarbonate filtration membranes as templates for the growth of Au nanotubes and nanowires [74]. In their electroless method, Au deposition began at the pore walls creating, at short deposition times, hollow Au nanotubes within the pores extended plating resulted in the formation of Au nanowires. Zhang et al. employed an electroless deposition method for the synthesis of Ag nanotubes using porous anodic aluminum oxide as templates [51]. Ag nanotubes with lengths over 10 μm were obtained in high yield.

In this chapter, we have investigated electroless deposition of Au on Si in the presence of surfactants with an objective of producing nanostructures without the use of templates. For this purpose, we

have made use of poly(vinylpyrrolidone) (PVP) and mercaptoundecanoic acid (MUA) as additives to the plating solution. The composition of films in such cases was obtained using X-ray photoelectron spectroscopy (XPS) and the morphology of the film with different concentrations of additives were examined. The conditions employed for preparing the different samples are listed in Table 3.1. In another process, the Si substrates were given an intermittent dip in octadecyltrichlorosilane in dry dichloromethane (OTS/DCM) which acted as a masking agent (see Table 3.2). The morphology of the resulting nanostructures has been studied using atomic force microscopy (AFM) and scanning electron microscopy (SEM). The crystallographic orientation of the nanostructures was examined by X-ray diffraction (XRD).

3.3 Experimental section

Cleaning of the Si wafer was done using the method described in Section 2.3.1. Two sets of samples were prepared: (i) in the presence of surfactants (PVP and MUA) as additives in the plating solution and (ii) by intermittantly dipping Si substrates in silane solution during plating.

(i) To study the influence of surfactants on the Au deposition, PVP (M_W $\sim$40,000 g mol^{-1}) and MUA were added in small concentrations under the standard plating conditions (0.1 mM KAuCl$_4$, 28 °C, 30 minutes). The concentration of PVP was varied from 0.005 to 0.1 mM (**1-4**, see Table 3.1) and of MUA, from 0.01 to 0.1 mM (**5-8**, Table 3.1) in the plating solution. As MUA is insoluble in water, ethanol was used as the solvent to dissolve

it (∼0.2 mL). Higher concentrations of MUA turned the solution turbid
because of poor solubility. The deposition on cleaned Si(111) substrates
was carried out for 30 minutes at room temperature except for the sample
where the deposition time was 120 minutes (**8**). After the deposition, the
substrate was washed with double distilled water and dried under flowing
argon. The films were characterized by XRD and AFM in the contact
mode. The PVP-Au samples were also subjected to XPS measurements to
study the binding of Au with PVP.

Table 3.1 Experimental parameters for electroless deposition of Au films
in the presence of additives.

Sample number	KAuCl₄ (mM)	Time of deposition (min)	Concentration of PVP (mM) MUA (mM)	
1			0.005	
2			0.01	
3			0.04	
4	0.1	30	0.1	
5				0.05
6				0.01
7				0.1
8		120		0.1

(ii) In another set of experiments, freshly etched Si(111) substrates
were dipped in the standard plating solution for a brief duration (2 or 5
s) in order to create discrete Au nucleation sites. The unreacted portions
of Si were further hydroxylated by treating with piranha solution (1:2
$H_2O_2{:}H_2SO_4$) at 80 °C for 10 minutes. The substrates were transferred

to an argon atmosphere in a desiccator for a dip in OTS/DCM, as OTS is moisture sensitive. The setup used for this experiment is shown in Figure 3.1. The desiccator contained two 50 mL beakers, one filled with OTS/DCM (5 mM) and the other, the standard plating solution. The nanostructured substrates were prepared with varying dip durations as listed in the form of flowchart in Table 3.2. The morphology of the substrates thus prepared was imaged using contact mode AFM and SEM imaging was also done for few samples.
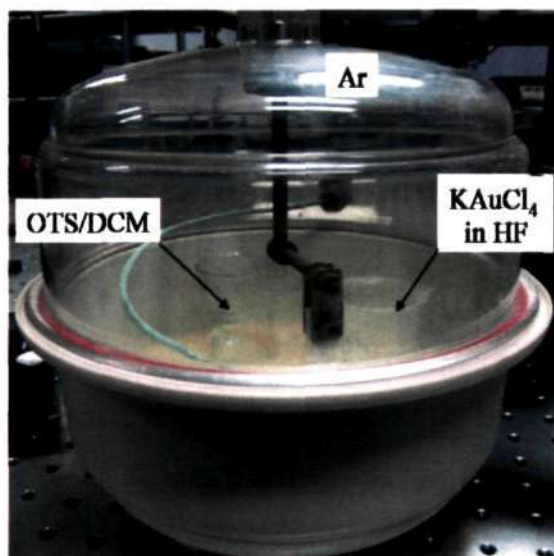
Figure 3.1   A photograph of the setup used to create Au nanostructures.

3.4   Characterization Techniques

The samples were characterized by X-ray diffraction (XRD), atomic force microscopy (AFM), X-ray photoelectron spectroscopy (XPS), scanning electron microcopy (SEM) and optical profilometry (OP). The details of XRD, AFM and OP are given in Section 2.3.3.
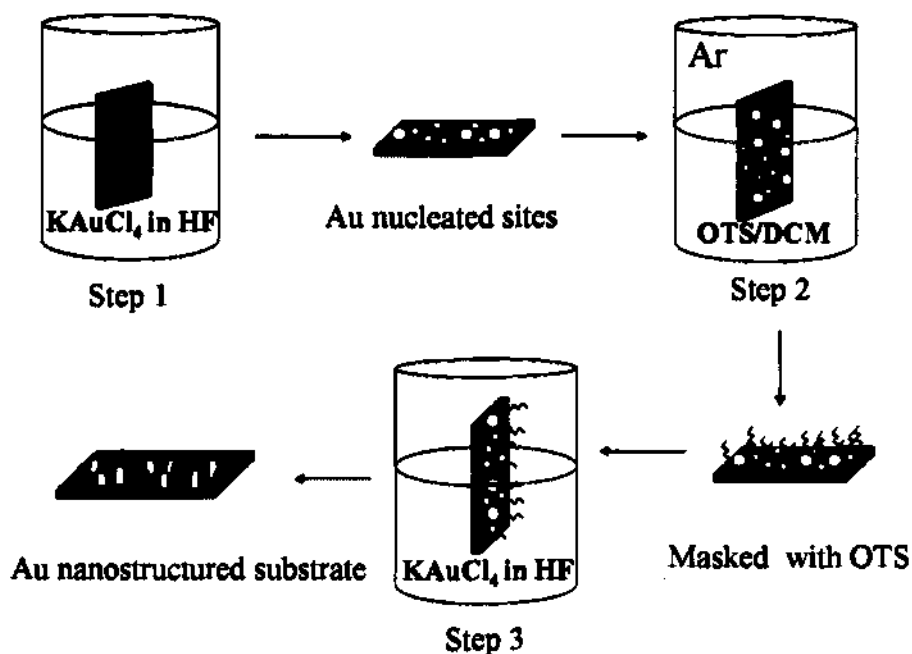
Figure 3.2 Schematic of the experimental procedure

X-ray photoelectron spectroscopy: XPS was measured using a VG scientific ESCALAB MK-IV spectrophotometer with X-ray source of Al K_α (1486.6 eV). The operating condition for recording was 10 kV and 10 mA, pass energy 25 eV with an operating pressure of 10^{-9} torr. The acquisition time is 120 seconds for all the samples. The reported binding energies are referred with respect to the Au ($4f_{7/2}$) level (84.0 eV).

Scanning electron microscopy: SEM images were obtained using LEICA S440i equipment. Energy dispersive analysis (EDX) was performed with a Oxford microanalysis group 5526 system attached to the SEM employing links (ISIS) software and a Si(Li) detector.

Atomic force microscopy: While a multimode AFM was routinely employed, for **10,** a CP-II AFM equipment (Veeco, USA) with 100 x 100

Table 3.2 Flowchart of sample preparation
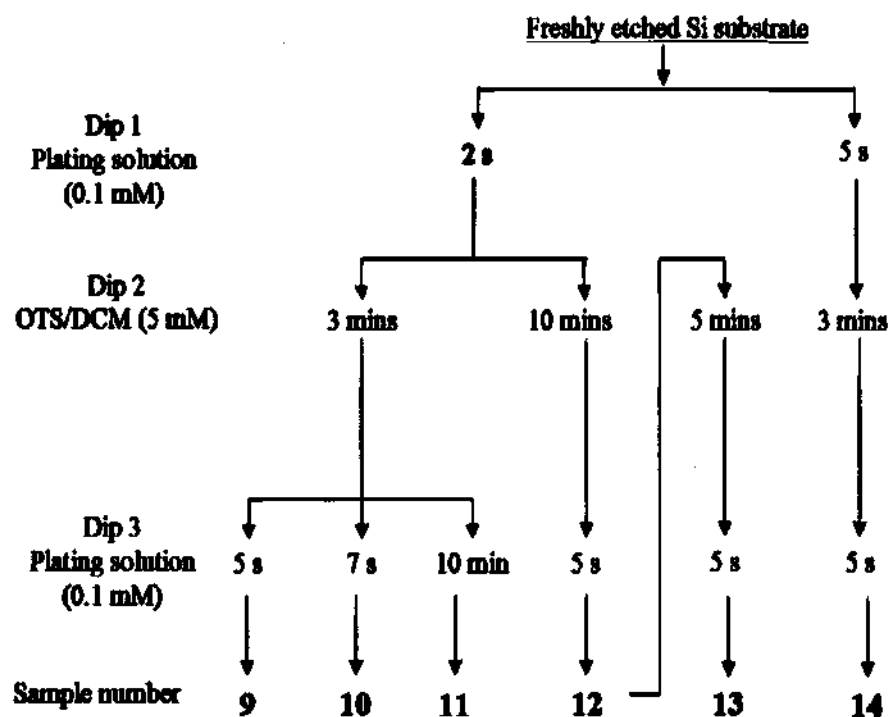
μm^2 scanner was used. A fractal analysis was carried out on this sample

using a software application provided with the instrument.

3.5 Results and Discussion

3.5.1 Additives in the plating solution

PVP as additive

We have made a detailed study of the influence of surfactants on

the Au deposition process. Figure 3.3 shows the XRD pattern obtained

for different concentrations of PVP in the standard plating solution.

At smaller concentrations of PVP, 0.005 and 0.01 mM (Table 3.1, **1**

and **2** respectively), the diffraction patterns resemble closely with those

obtained films without any additive (see Figure 2.1). In other words, the

presence of PVP brings no noticeable change in the diffraction patterns at

such low concentrations. In contrast, for higher concentrations 0.04 mM

(3 and 4), there is hardly any intensity in the diffraction pattern, as if

the deposition process itself is hindered.   The nature of the deposited

Figure 3.3 XRD patterns of Au films obtained with different con-
centrations of poly(vinylpyrrolidone) (PVP) under the standard plating
conditions, (0.1 mM KAuCl$_4$, 28 °C, 30 min).

material became more evident from AFM and XPS analysis shown in

Figures 3.4 and 3.5.   The AFM images in Figure 3.4 reveal granular

structure of the deposited material.   The images obtained with lower

concentration of PVP, 1 and 2 (see Figure 3.3a and b) appear similar

to the one without PVP (see Figure 2.6a). As the concentration of PVP
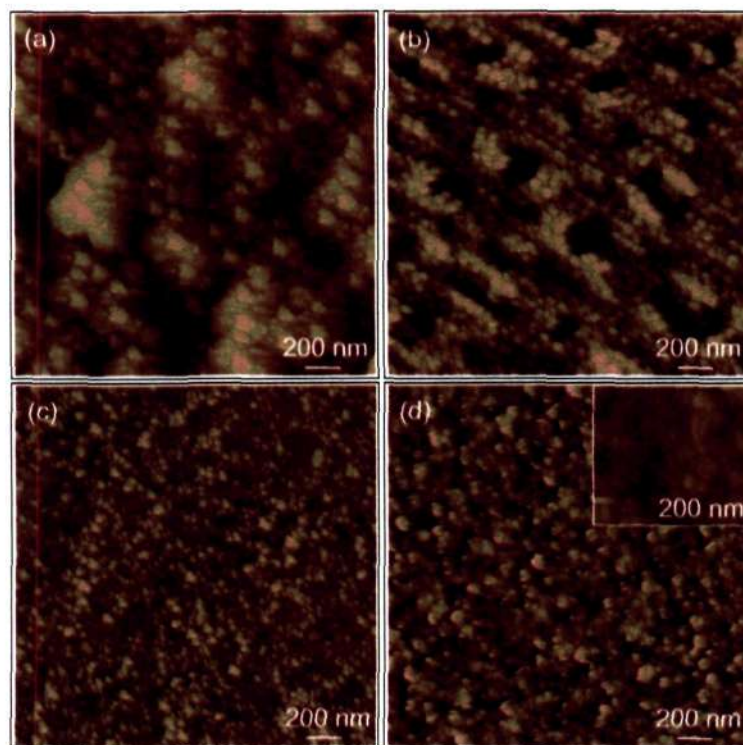
Figure 3.4   Tapping mode AFM image of Au films for a PVP concentration of (a) 0.005 mM, (b) 0.01 mM, (c) 0.04 mM and (d) 1 mM. Inset shows an image from a smaller scan area.
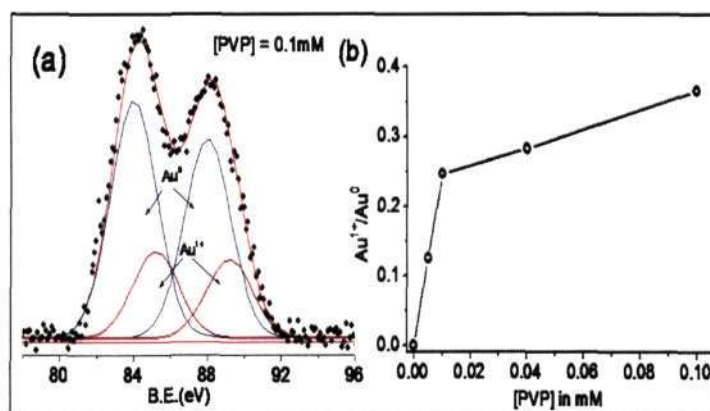
Figure 3.5   Au(4f) core-level spectrum of the film obtained with 0.1 mM PVP concentration. The presence of Au^{1+} and Au^0 species is revealed following deconvolution. Inset shows variation in Au^{1+}/Au^0 with PVP concentration.

is increased in the standard plating solution, the film becomes more granular with size in the range of 80-140 nm for **3** and **4** (Figure 3.4c and d). Each granule appears as an aggregate of particulates, each presumably only a few nanometers in size (see inset in Figure 3.4d).

As no diffraction intensity was observed for **3** and **4** (see Table 3.1), XPS measurements were performed to understand the nature of Au species. The Au(4f) core level obtained from the films indeed revealed the presence of Au^0 and Au^{1+} species as illustrated in Figure 3.5 for a PVP concentration of 0.1 mM (**4**). Clearly, the Au^{1+} species arises due to capping of PVP due to surface Au-N or Au-C bonds [75]. The Au^{1+} concentration in the film increases with increase in the concentration of PVP in the standard plating solution as shown in the inset of Figure 3.5. It is possible that PVP arrests the growth of Au particulates, more so when it is in higher concentrations, rendering the film X-ray amorphous. The films with PVP as additives appeared lustrous when compared with pure Au films. This may be due to the presence of Au^{1+} state.

MUA as additive

With the addition of 0.1 mM MUA to the standard plating solution, the (111) orientation of the film was unaffected as shown in Figure 3.6 (**5**, see Table 3.1). We have observed only a small drop in the intensity of the diffraction peak with increasing concentration of the additive. However, the plating solution turned turbid as the concentration of the additive was increased beyond 2 mM. This may be due to the poor solubility of MUA in the plating solution. The corresponding AFM images are shown
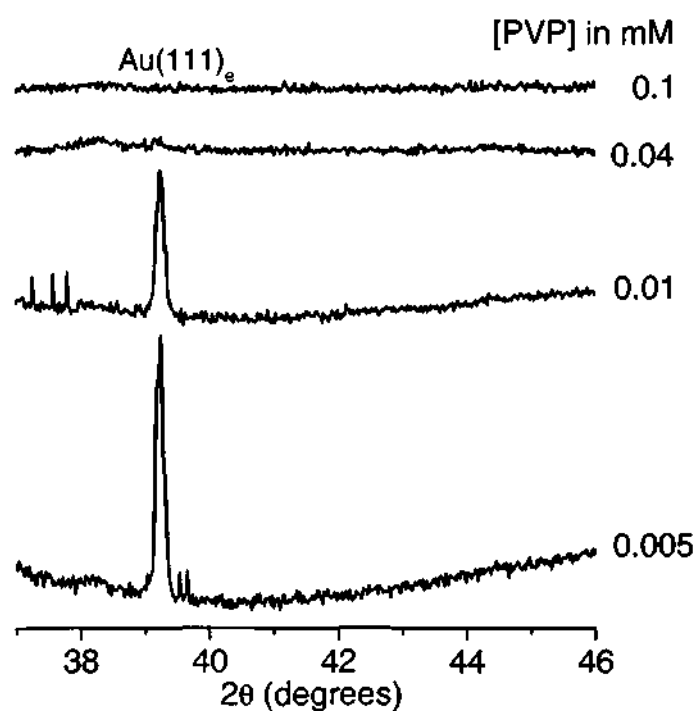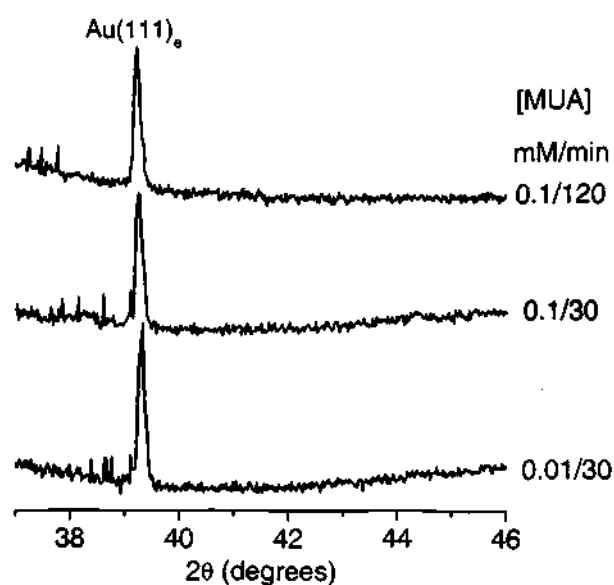
Figure 3.6   XRD patterns of Au films obtained with different concentrations of mercaptoundecanioc acid (MUA) under the standard plating conditions. (0.1 mM $KAuCl_4$, 28 °C, 30 min).

in Figure 3.6. The films exhibit a different morphology as compared to the films with PVP as the additive (see Figure 3.4). In this case, we observed islands of dimensions 200-400 nm clearly standing out from the rest of the film. From the z-profile analysis in Figure 3.7c, we find that the islands are quite flat with rms roughness of ~1.5 nm. This may be compared with the roughness values (10-15 nm) from other regions in the film. The height of the islands is in the range of 25-35 nm, matching with the average thickness of the film. While the exact role of MUA in the formation of flat islands is unclear, it appears that MUA by way of forming a self-assembled monolayer induces the formation of flat regions with (111) orientation. It is interesting to note that as the concentration of MUA is increased, the size of islands also increases.
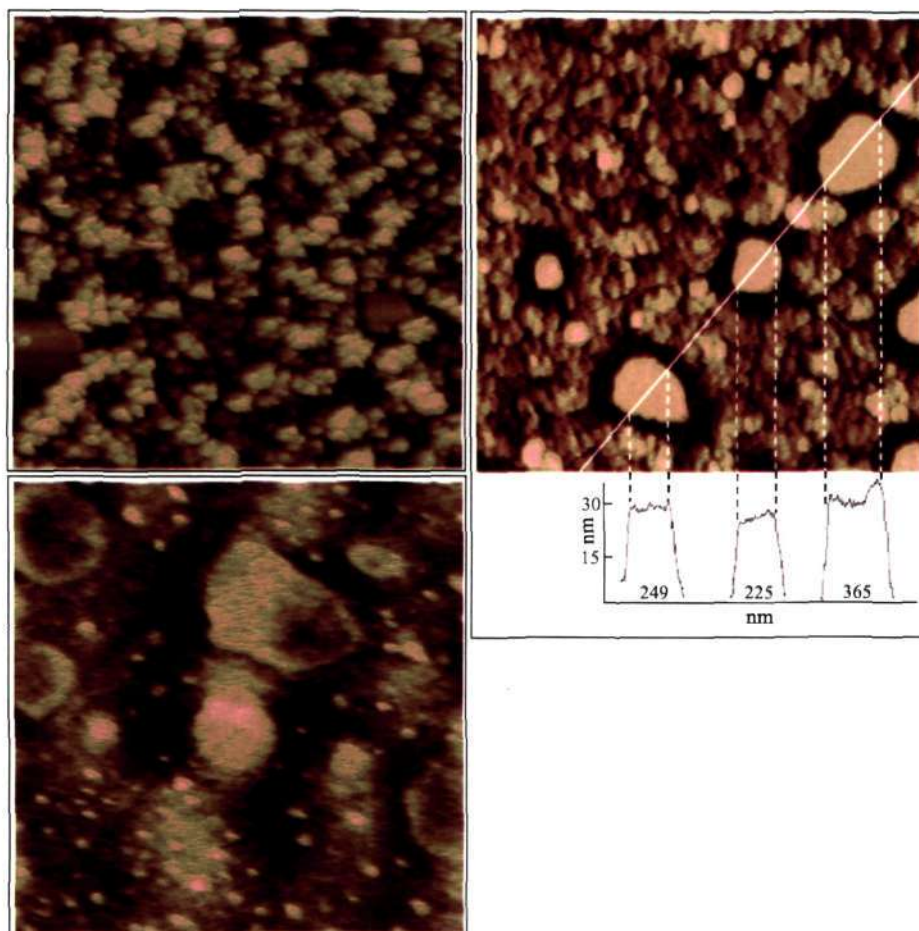
Figure 3.7   Contact mode AFM image (2 x 2 μm^2) showing distinct gold islands for different concentration and time durations of MUA (a) 0.01 mM and 30 minutes, (b) 0.1 mM and 30 minutes with z-profiles of the islands and (c) 0.1 mM for 120 minutes of deposition.

3.5.2   Intermittent dips in OTS during plating

The results discussed below pertain to Au nanostructures obtained by carrying out an intermittent dip in a masking agent, OTS in dry DCM (5 mM). Initially, a clean Si substrate was dipped in the standard plating solution for 2 seconds to initiate some Au nucleation sites. Following a dip in OTS/DCM, we intended to cover the exposed Si surface with OTS [76,77] such that during the next dip in the plating solution, only

preformed Au nucleation sites are allowed to grow. As Au ions can get reduced only on bare Si surface, silanization of Si surface acts as a mask for Au deposition, thereby facilitating selective deposition of the metal. Thus, a 3 minutes dip in OTS/DCM followed by a 5 seconds dip in the plating solution (**9**, see Table 3.2) produced discrete trapezoidal islands with lateral dimensions ~300-400 nm and height ~50-80 nm as shown in Figure 3.8. It is interesting that the islands retain the (111) epitaxial orientation as observed in continuous films (see Figure 2.1).

Increasing the duration of the initial dip in the plating solution from 2 to 5 seconds did not help in increasing the density of the islands instead the deposition produced dense Au aggregates on the substrate (**14**) as shown in the inset of Figure 3.8.   With the durations of dip 1 and 2
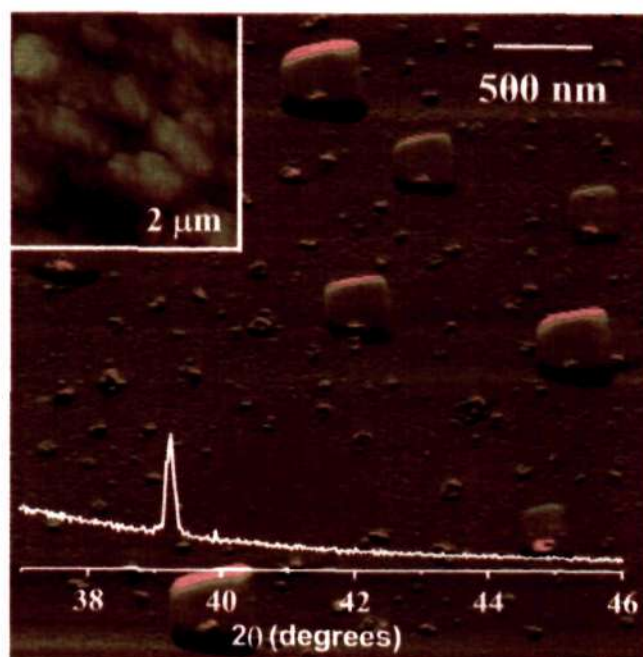
Figure 3.8   (a) Contact mode AFM image of Au islands deposits on Si(111) substrate obtained after an intermittent dipping in OTS/DCM along with the XRD pattern (OTS/DCM) (**9**). Inset showing 2 x 2 μm^2 area of the substrate with Au nucleation time as 5 seconds (**14**)
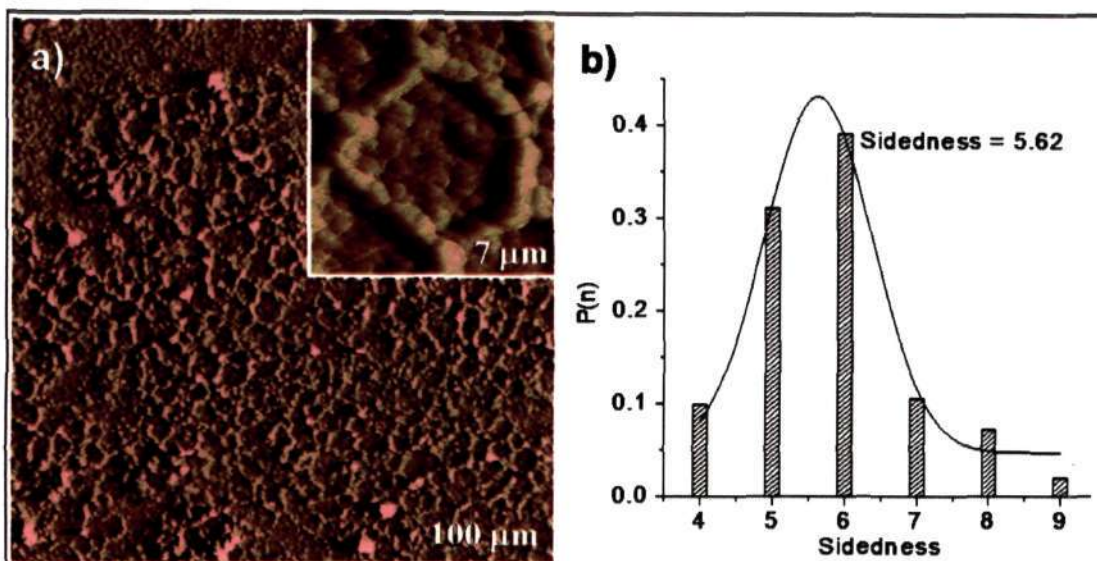
Figure 3.9 (a) Contact mode AFM images showing cellular network (**10**).
Inset showing a distorted hexagon from a small area scan. (b) Histogram
of the polygon side distribution fitted with guassian distribution.
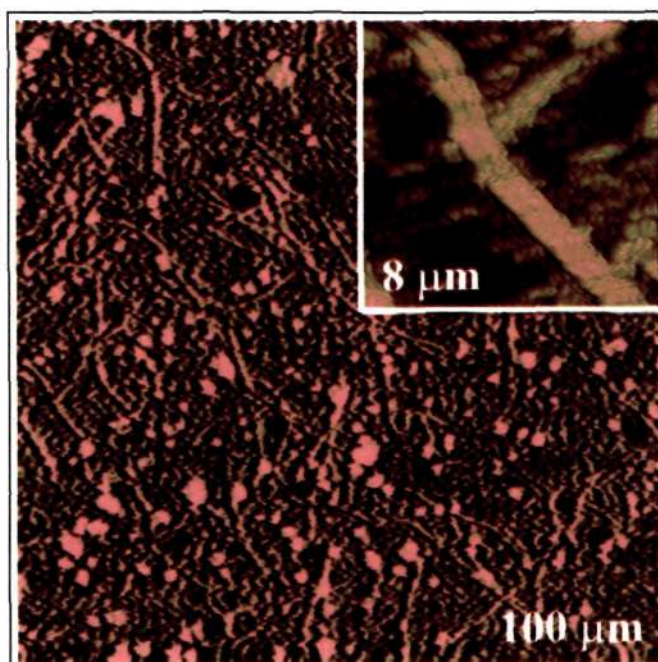
Figure 3.10 Topography of the Au deposits when the final dip is
extended to 600 s,(**11**).   Inset shows an image of a Y-shaped
nanostructure.

maintained at 2 seconds and 3 minutes respectively, we have varied the

duration of the final dip in the plating solution in order to study further

growth of Au islands. With a 7 seconds dip (10), the deposition yielded an interesting cellular network structure as shown in Figure 3.9. This may be contrasted with Au islands shown in Figure 3.8. It appears that the islands grow laterally in specific directions forming interconnected cellular network. An added factor could be that the new nucleation sites may continue to germinate as OTS coverage from 3 minutes dip may not be quite dense. This is apparent from the small outgrowths between the islands in Figure 3.8.

The cellular network consists of interconnected polygons of different sidedness. One such polygon (distorted hexagon) is shown in the inset of Figure 3.9a. We have carried out a tessellation analysis of the cellular network. The histogram in Figure 3.9b gives a mean value of 5.62 for the polygon sidedness. This value is close to 6, expected of an infinite cellular network [78]. Other instances of such cellular networks include colloidal particle foams [12,78,79]. Further increase in the final deposition time to 10 minutes (11) resulted in the formation of highly interlinked channels and cavity-like structures, as shown in Figure 3.10. Thus, the islands instead of growing in height seem to interlink leaving out cavities occupied by OTS molecules. A zoomed-in region in the inset highlights a Y-shaped nanostructure (see Figure 3.10).

In an effort to avoid the small outgrowths resulting from unsaturated coverage of OTS (see Figure 3.8), we increased the duration of the OTS/DCM dip to 10 minutes (Figure 3.11). The AFM image of 12 in Figure 3.11a shows the formation of well-defined islands of Au without any

outgrowth. Under the given reaction conditions, a 10 minute dip appears crucial unlike on a neat Si surface [76,77]. The islands exhibited (111) orientation as evident from the XRD pattern. A z-profile analysis was carried out (a typical one shown in Figure 3.11a) on a number of islands in terms of their heights, areas and the nearest neighbor distances. The histograms thus obtained are shown in Figure 3.11b. From the top histogram, we find that majority (50%) of the islands possess height in the range of 60-80 nm range while few of them (15%) are as tall as 100 nm. The distribution in the areas of the islands is found to be quite narrow, as shown in the histogram in the middle. About 50% of islands tend to have an area of 15×10^4 nm^2, while the average area occupied by an island is $\sim 17 \times 10^4$ nm^2. The islands are more frequently separated from each other by a 300-400 nm range as shown in the histogram at the bottom of the figure. A small fraction (12%) of them is separated by a shorter distance of around 150 nm. From the results shown in Figures 3.5, 3.7 and 3.11a, we observe that both the methods - using MUA additive and an intermittent dip in OTS/DCM are useful in obtaining well-formed Au islands on Si substrates. The latter has the advantage that there is no unwanted metal deposition. Further, compared to literature procedures on island structures [68-70], our method is simple and straightforward. A substrate with such well-defined metal islands may find potential applications for patterned growth of nanotubes, etc.

In order to compensate any possible loss or displacement of OTS molecules during treatment with the plating solution, **12** was dipped
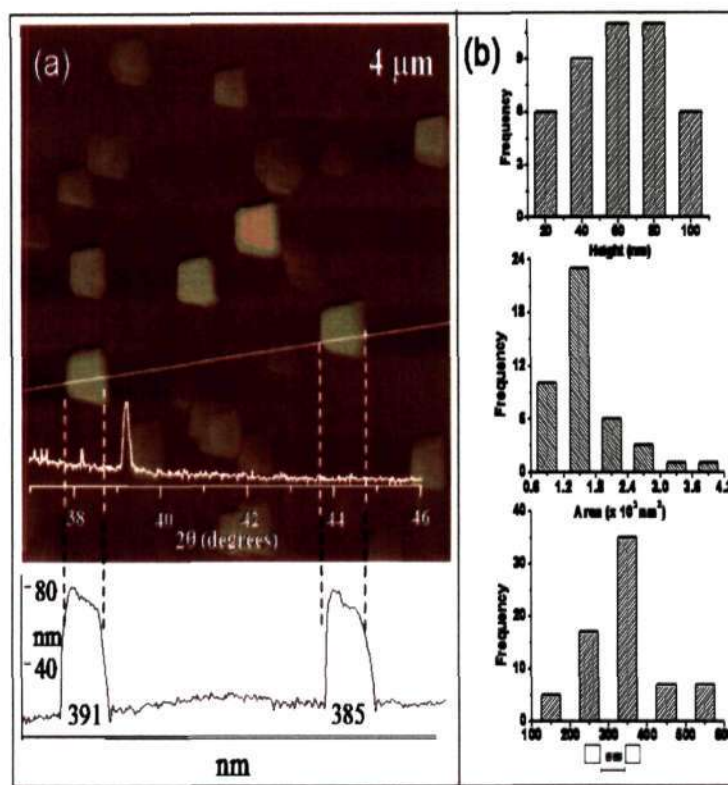
Figure 3.11   (a) Contact mode AFM image of Au islands on Si(111) for **12**.
The XRD pattern of the deposit along with z-profile analysis is also shown.
(b) Histograms showing height, area and nearest neighbor distances of
the Au deposits.

once more in OTS/DCM (**13**). Following this, interestingly, the islands

exhibited further growth into densely packed Au nanowires as shown in

the SEM image in Figure 3.11. The AFM image in the inset shows that

they possess diameters in the range 300-400 nm, comparable with the

dimensions of the islands formed in the first stage (see Figure 3.10). The

Au nanowires reported here may be contrasted with those from template-

assisted methods [51,74].
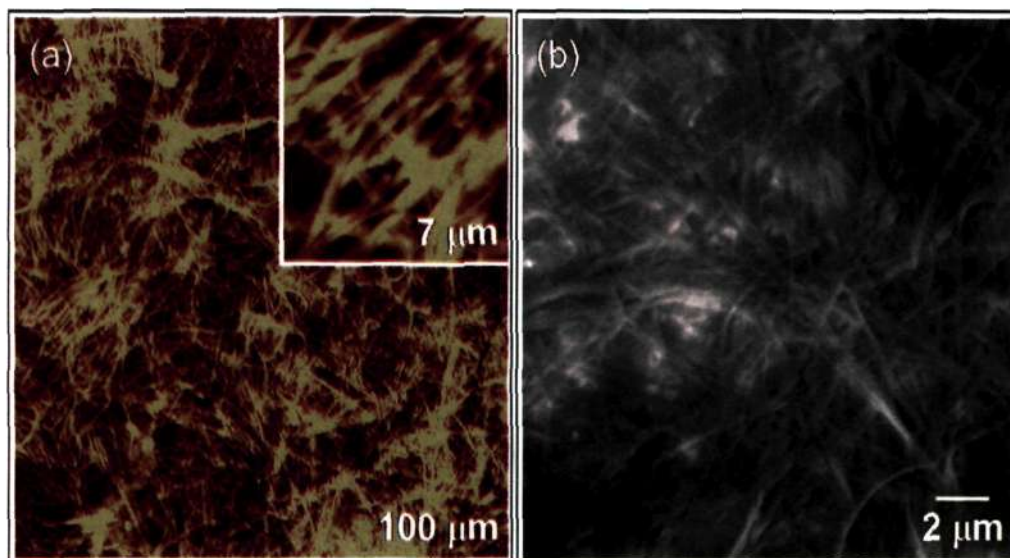
Figure 3.12   (a) Contact mode AFM image of the nanowires of **13** (dipped twice in OTS/DCM) showing Au nanowires. Inset shows an image from a smaller scan area and (b) SEM image showing nanowires.

3.6 Summary

We have found that PVP and MUA as additives to the plating solution, greatly influence the morphology of the electrolessly deposited Au films. Poly(vinylpyrrolidone) (PVP) produces X-ray amorphous films containing Au^{1+} species proportional to the PVP concentration as evidenced by X-ray photoelectron spectroscopy. Mercaptoundecanoic acid (MUA), on the other hand, produces large flat islands of Au.

In another study, the deposition process has been interrupted by intermittent dips in OTS/DCM to mask unreacted Si surface. By varying the time durations of the dips, Au nanostructures in the form of isolated islands, cellular networks and nanowires have been obtained. Thus, the study opens up new avenues for Au nanostructuring. This method could serve as a means of obtaining patterned substrates potentially

useful as catalysts for the growth of other nanostructures such as carbon nanotubes. They could also be used as nanoelectrode arrays.

Chapter 4

SERS studies on electrolessly deposited Au at the C/Si interface

4.1 Scope of study

In this chapter, we have investigated the nature of electroless deposition of Au on Si substrates precoated with overlayers of carbon. While there have been reports on the deposition of Au on carbon by electrochemical methods, to our knowledge, no systematic study has been carried out during the electroless plating. Herein, we not only describe our experimental results on the surface morphology of the gold and carbon deposits from the electroless process, but also report a systematic study on the usage on these substrates for Surface Enhanced Raman Scattering (SERS) measurements.

4.2 Introduction

Surface Enhanced Raman Scattering (SERS) is emerging as an important tool in biochemistry and medicine for trace analysis of molecules [80]. When adsorbed on metallic nanostructures like colloids, molecules exhibit an enhanced Raman signal [81,82], usually of several orders of magnitude higher compared to free molecules. Although colossal enhancement has been achieved using Ag and Au colloids [83], the usage of sols suffers from shortcomings such as their inherent instability, poor reproducibility and the necessity of external agents [80,84]. In this context, solid substrates coated with Ag or Au have been more promising [85-89]. Between the two, Au is biocompatible and is therefore preferred to Ag in spite of its lower ability to enhance the Raman signal [80]. A wide variety of Au substrates have been tried out for SERS. Typical examples include nanoparticle aggregated films [90-95] and arrays [96-98] and more recently lithographically laid 2-D arrays of nanoparticles on smooth films [99-101] with enhancement factors varying from 10^5 to 10^8 [90-101]. The SERS activity on these kind of substrates primarily depends on parameters such as surface morphology, particle size, interparticular spacing and surface plasmon coupling capabilities [102].

We considered it interesting to investigate SERS activity on nanogranular Au films prepared by electroless deposition in the presence of carbon overlayer. As first part of the study, Si substrates precoated with carbon layer of different thicknesses were dipped into the plating solution for different time intervals. The resulting substrates were carefully examined

by a variety of microscopy and spectroscopy tools. A few of the substrates were later subjected to SERS measurements.

4.3 Investigation of the Au-C/Si substrates

4.3.1 Experimental Section

The Si(100) substrates were cleaned according to the procedure described in Section 2.3.1. Carbon coating on these substrates was carried out by pulsed laser deposition (PLD). A frequency tripled pulsed Nd:YAG laser (Quanta-Ray GCR-170, Spectra-Physics, USA) with pulse energy 200 mJ and repetition rate of 10 Hz was used for the ablation of a graphite target. A convex lens of 30 cm focal length was used to focus the laser beam on to the target, through a quartz window fastened to the deposition chamber, held at 10^{-6} torr. The substrate was placed directly opposite to the target at 5 cm. Deposition of graphite was carried out for 5, 15, 30 and 60 minutes. After the carbon deposition, the substrates were electroless deposited with Au. For this purpose, 5 mL of 0.1 mM plating solution ($KAuCl_4$ in 5 M HF) was taken in Teflon container and the deposition was carried out for different time durations (5-120 minutes). A few depositions were carried out without a carbon overlayer. Following the Au deposition, the substrates were carefully rinsed with double distilled water and dried under flowing argon.

The thickness of the film was measured after both carbon and Au depositions using an optical profiler (OP). The desired step for OP measurement was created by masking a portion of the substrate with

a teflon tape during deposition. Raman spectroscopy measurements on the carbon overlayers were carried out using a HR 800 Horiba Jobin Yvon with LabRaM spectrometer and LABSPEC software. The chemical state of Au in Au-C/Si samples was analysed using XPS. The morphology of the film was analyzed using AFM.

4.3.2 Results and Discussion

In Figure 4.1, profilometric image of carbon overlayers on Si obtained after 5, 15, 30 and 60 minutes of deposition are shown. The steps are clearly visible and the line profile analysis gave estimates for the step heights of 12, 30, 90 and 190 nm respectively. We also observe from the image, increased roughness of the deposited carbon. Accordingly, the estimated rms roughness values turn out to be 9, 23, 37 and 45 nm respectively. Raman spectroscopy measurements have been carried out on the deposited carbon overlayers (Figure 4.2). From Figure 4.2a, we observe that the spectra contain two broad bands at $\sim$1355 and 1575 cm^{-1} and their intensities increase with the deposition time. The broad band at 1355 cm^{-1} is the peak D corresponding to disordered graphite and that at 1575 cm^{-1} corresponds to the peak G of the single crystalline graphite [103,104]. More specifically the G mode arises from stretching of any pair of sp^2 sites, whether in rings or chains (see schematic in Figure 4.2a), while the D mode is the breathing mode of sp^2 sites in rings not chains. Thus, the ratio of I(D)/I(G) can provide a useful measure of the disorder in the deposited carbon overlayer. In Figure 4.2b, we have shown how the ratio, I(D)/I(G) increases with increased

carbon deposition suggesting the presence of amorphous carbon at longer deposition times. The disorder increases rapidly beyond 30 minutes of deposition. This goes well with the roughness values observed in our profilometric measurements.
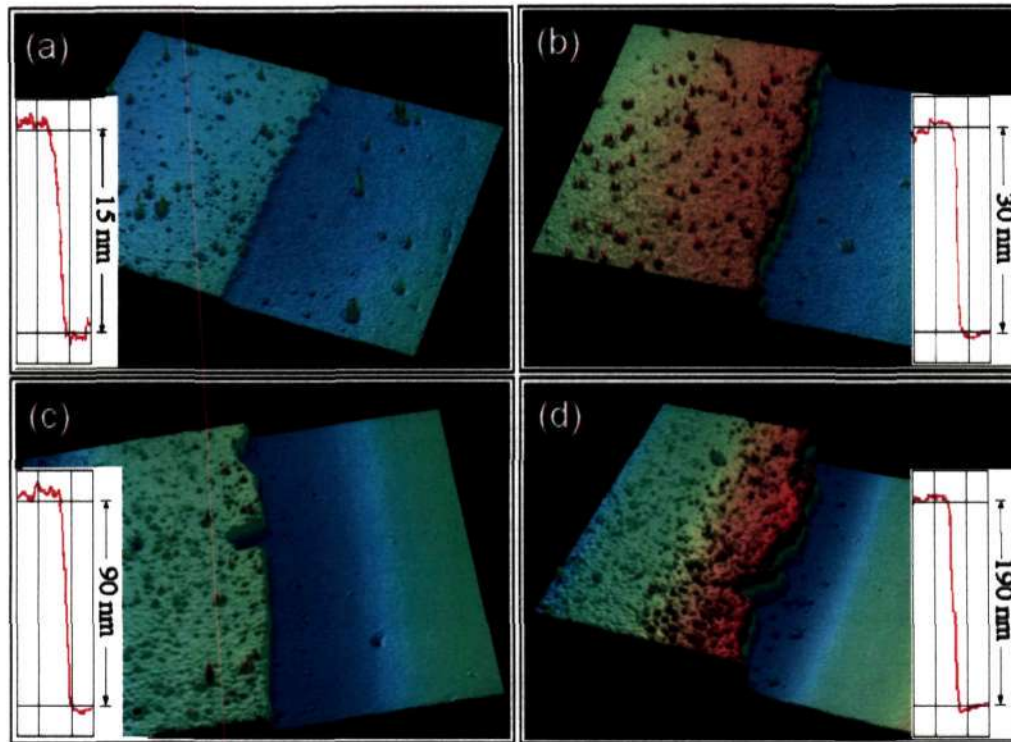
Figure 4.1 Profilometric measurements on carbon overlayers obtained by ablating graphite on Si(100) substrates for (a) 5 min, (b) 15 min, (c) 30 min and (d) 60 min. The corresponding line profiles showing the step heights are also shown.

The optical profilometry measurements were carried out across the steps 1-2, 2-3, 3-4 and 1-4 as shown in Figure 4.3. The regions, 1-4, are clearly discernible from the photograph of the substrate shown in the center of the figure. The step 1-2 (Figure 4.3a), due to the deposited carbon, measures 90 nm consistent with Figure 4.1c. However, the boundary between the regions 2 and 3 failed to exhibit a clear step (see
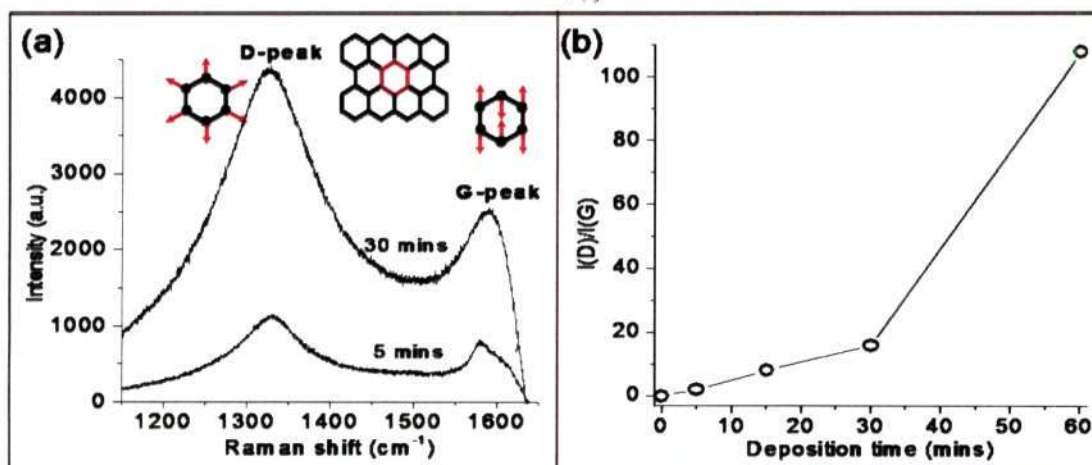
Figure 4.2 (a) Raman spectra of carbon overlayers with varying deposition times, 5 and 30 minutes. Vibrational modes associated with D and G peaks are shown pictorially. (b) A plot showing the variation in the ratio, I(D)/I(G) with the deposition time.

Figure 4.3b), implying that the Au deposition in the region 3 over carbon does not add to the film thickness. On the contrary, Au deposited on bare Si (region 4) distinguishes itself more clearly (see Figure 4.3c and d). Although uptake of Au on carbon is vivid from the photograph shown, the absence of a step between the regions 2 and 3 is a clear indication that the deposited Au is embedded within the porous layer of amorphous carbon.

In order to ascertain the exact chemical nature of the deposited Au on C/Si substrates, we have carried out detailed analysis of the Au(4f) core level spectra. In Figure 4.4 are shown typical spectra along with the deconvoluted peaks corresponding to various Au species, Au^0, Au^{1+} and Au^{3+} with the $4f_{7/2}$ binding energy at 84, 85.5 and 87 eV respectively. From Figure 4.4a, we see that in the absence of carbon on Si, the spectrum is narrow and symmetric containing only
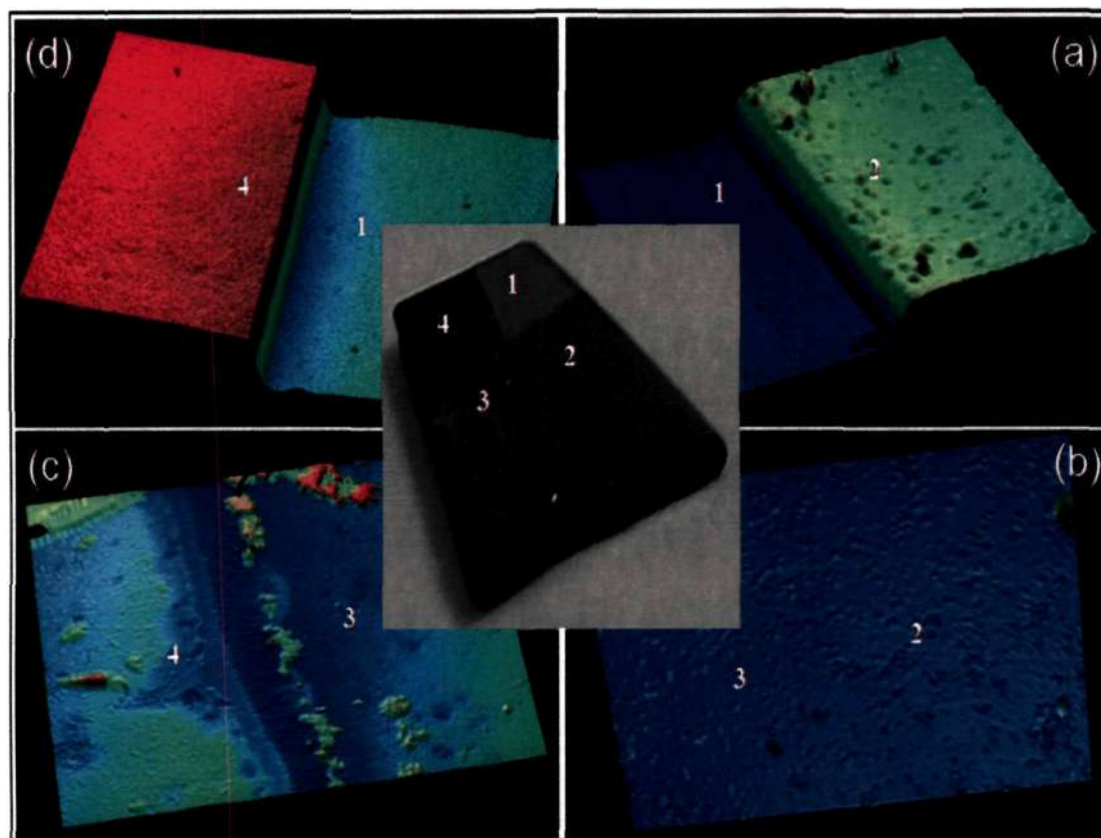
Figure 4.3 Profilometric measurements across different regions on the Si substrate (a) Si(1) - C/Si(2), (b) C/Si(2) - Au-C/Si(3), (c) Au-C/Si(3) - Au/Si(4) and Si(1)- Au/Si(4). Carbon deposition was carried for 30 minutes in regions 2 and 3, followed by Au deposition for 120 minutes in regions 3 and 4, by selective masking. The inset at the centre shows a photograph of the substrate.

Au^0 species. With precoated carbon of 15 and 45 nm thickness, the spectra appear significantly broader with enhanced intensity at higher binding energies.   The spectral deconvolutions revealed the presence of considerable amounts of Au^{1+} and Au^{3+} species.   The Au^{1+} and Au^{3+} can originate from a surface gold carbide species.   For higher carbon film thickness of 90 nm, the spectral intensity was quite low and $4f_{7/2}$ position was shifted to 84.8 eV. The spectra in Figure 4.4b exhibit increased intensity with increasing Au deposition time from Si
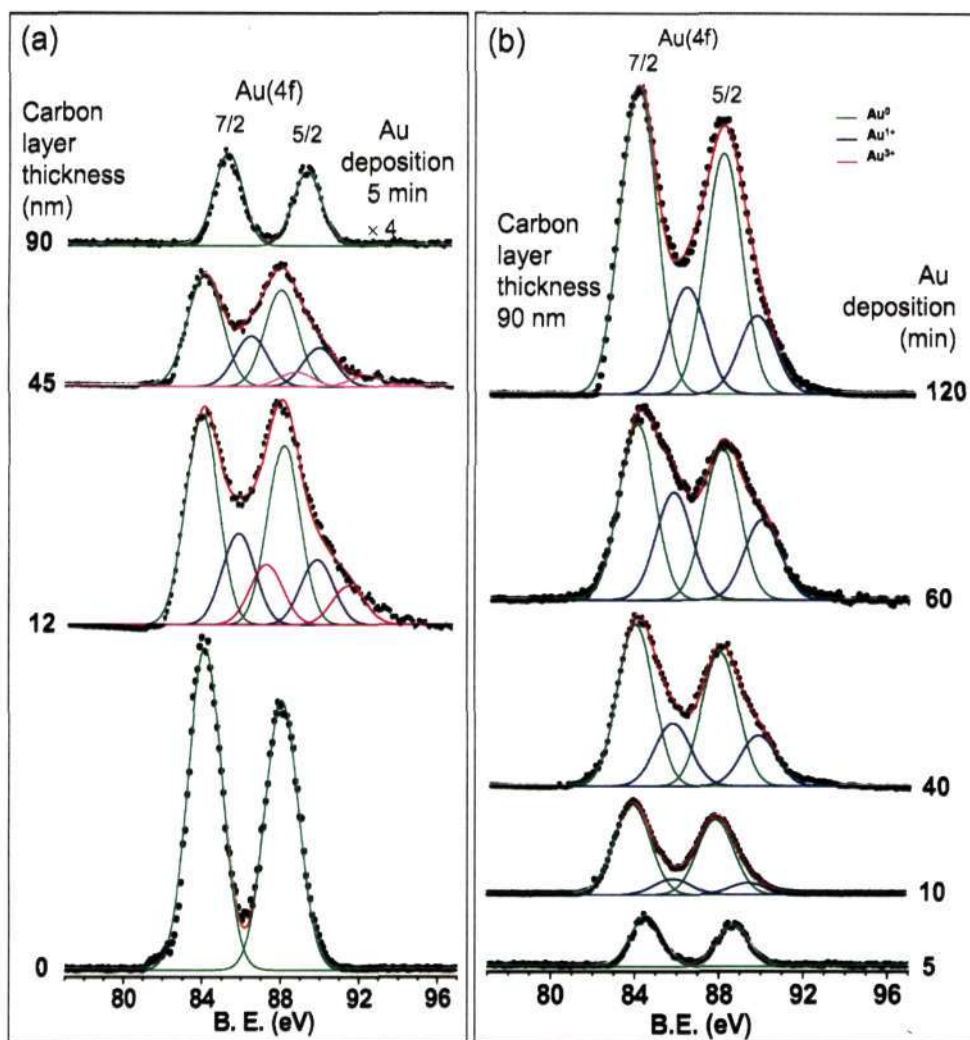
Figure 4.4   Au 4f core level spectra along with the deconvoluted peaks corresponding to Au^0, Au^{1+} and Au^{3+}, from (a) substrates obtained after 5 minutes of Au deposition over carbon layers of different thickness. (b) substrates obtained after different Au deposition times over carbon layer of 90 nm thick.

substrates, each precoated with a 90 nm carbon overlayer. The spectra do exhibit broadening due to the presence of Au^{1+} species as illustrated from the deconvolutions. The intensity of the deconvoluted Au^{1+} peak increases with the Au deposition time. It may be noted that C(1s) spectra from the above substrates exhibited peaks at 284 eV, characteristic of

amorphorized carbon.
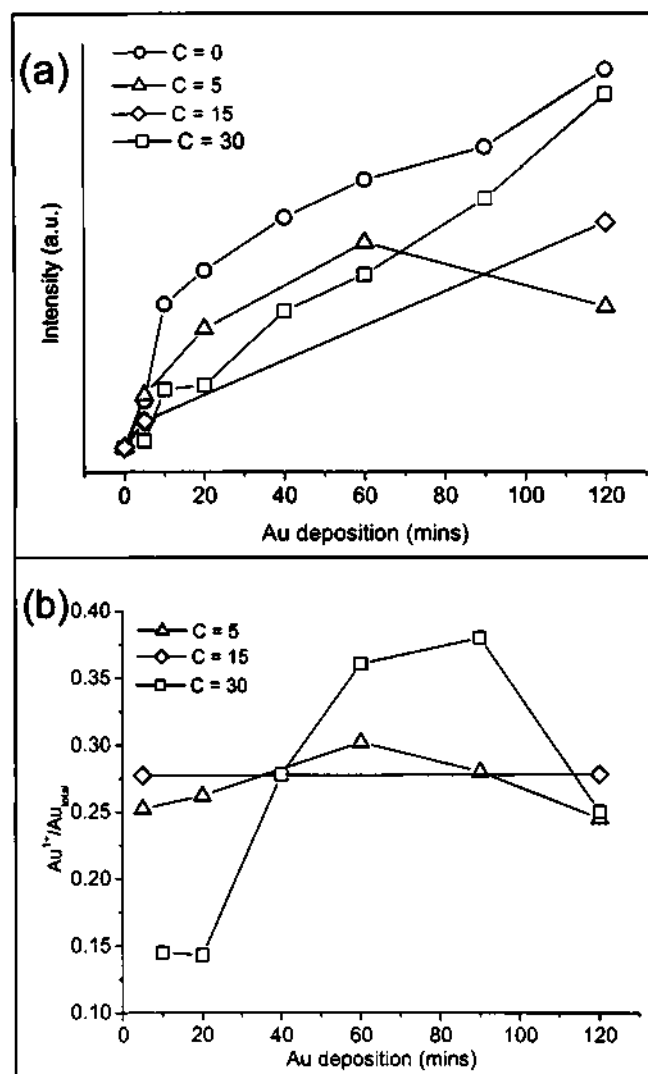
Figure 4.5 (a) Variation in the total spectral intensity and (b) variation in the Au^{1+}/Au_{total} ratio with the Au deposition time over carbon layers of varying thicknesses.

A quantitative analysis of the core level spectra has been carried out (Figure 4.5). In the absence of the carbon overlayer, the uptake of Au as seen from the spectral intensity is rapid during the first 10 minutes but slows down and becomes linear with the deposition time. However, the Au uptake is relatively less in the presence of carbon overlayers. What

is noteworthy is the variation in the Au uptake on the carbon overlayer of 90 nm thick, which though considerably less at shorter deposition times, nearly approaches that obtained with no carbon overlayer on the substrate. It appears that beyond 60 minutes of the deposition, the pores get interconnected by the metal all the way down to Si substrates catalyzing the Au reduction process itself. From Figure 4.5b, in the case of 90 minutes of Au deposition, we observe that the relative proportion of Au^{1+} species increases upto 0.38 but decreases to 0.25 for 120 minutes of the deposition. The latter behavior may be associated with the enhanced metal reduction. On the contrary, the proportion of Au^{1+} species vary less significantly ($\sim$0.27) with Au deposition time for carbon overlayers of lesser thicknesses. For substrates without carbon overlayers, the Au^{1+} species was absent.

The morphology of the deposited metal was examined by AFM. As an example, we show in Figure 4.6, AFM images of the substrates with a carbon overlayer of 15 nm subjected to Au deposition for 20, 60 and 90 minutes, respectively. In Figure 4.6a, the deposited metal is clearly identifiable as islands (100-150 nm) over a smooth background of the carbon film. With increase in the deposition time, 60 and 90 minutes, the islands become increasingly dense. With 90 minutes of deposition (Figure 4.6c), the Au islands are more regularly shaped but somewhat smaller in size (70-90 nm).

We have shown in Figure 4.7, AFM images of the Au-C/Si substrates with varying thickness of the underlying carbon layer. In all the cases,
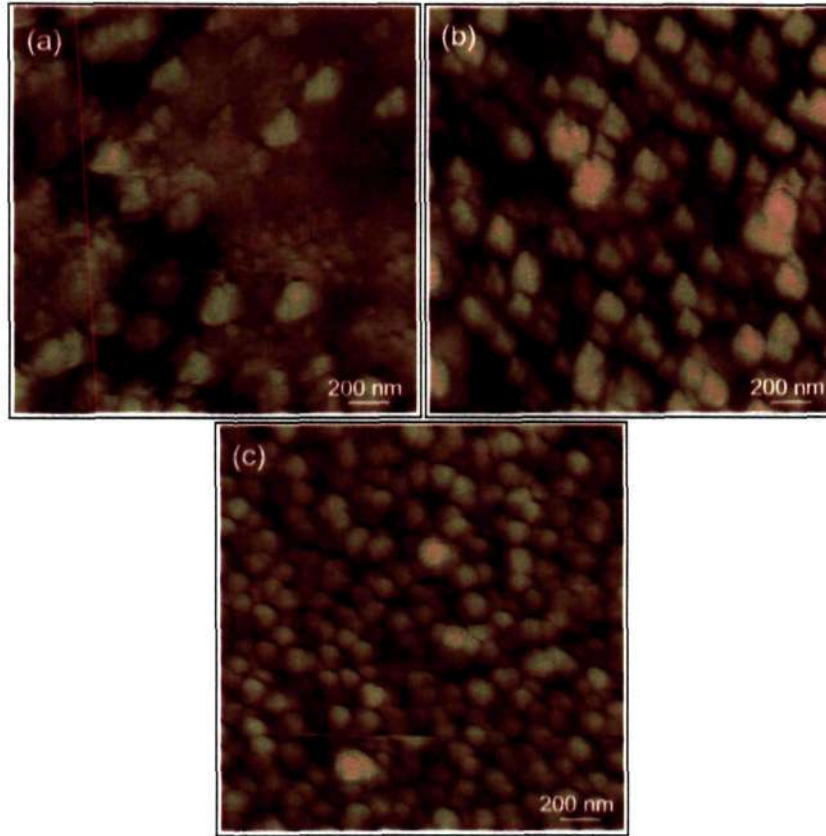
Figure 4.6   AFM images (1 x 1 μm^2) showing the morphology of the metal deposited on a 15 nm thick carbon overlayer for Au deposition times of (a) 20 mins, (b) 60 and (c) 90 mins.

Au deposition was carried out for 120 minutes. From the figure, we see that the substrates consist of close-packed Au granules of uniform size. However, the size of the granules is different among the various substrates. While the substrate with no carbon (Figure 4.7a), contains Au granules in the range of 260-280 nm, those covered with carbon prior to Au deposition possess granules of much smaller size. The size ranges of the granules estimated for these substrates with carbon overlayer thicknesses of 15, 45, 90 and 190 nm are 80-140 nm, 50-80 nm, 30-60 nm and 40-80 nm respectively. We also observe that the big sized granules in Figures 4.7a and b appear glued to each other while those
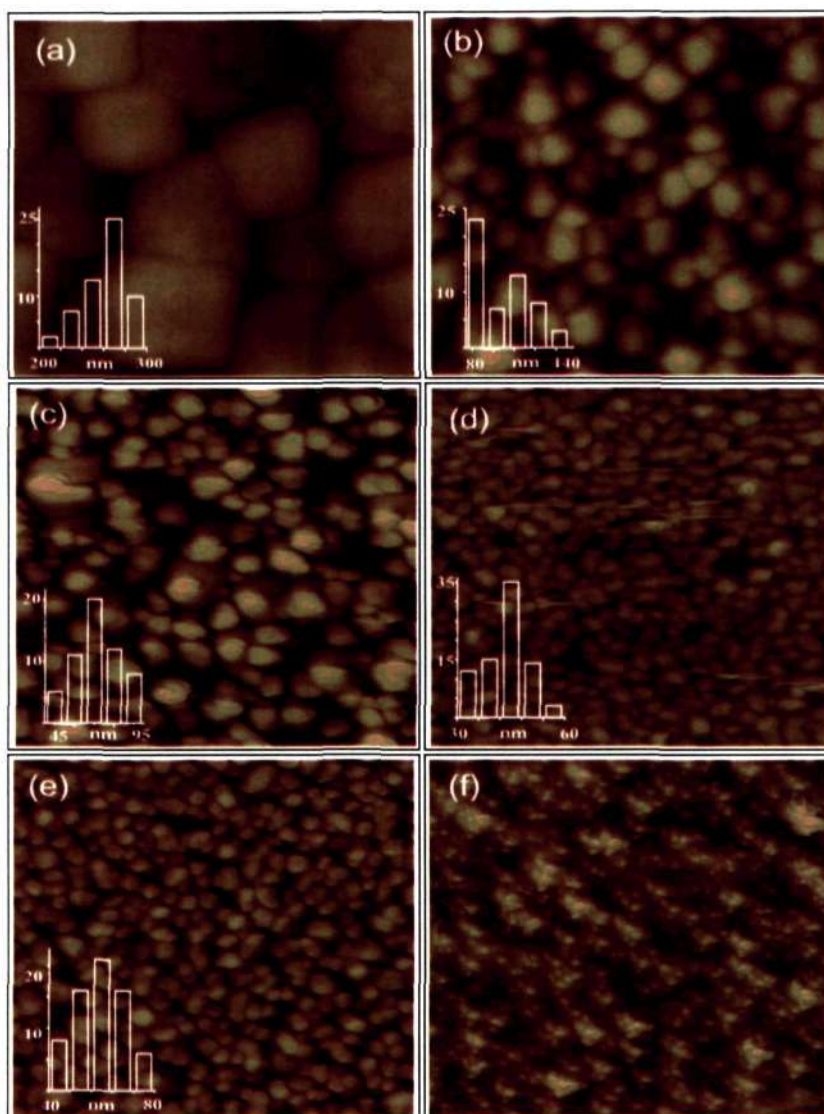
Figure 4.7   Contact mode AFM images (2 x 2 μm^2) of Au deposited on Si(100) substrates covered with varying carbon overlayer thicknesses (a) 0 nm (b) 15 nm (c) 45 nm (d) 90 nm (e) 180 nm with Au deposition time as 120 minutes. (f) Substrate with carbon overlayer thickness as 90 nm by the Au deposition was carried out in two steps (40+80) minutes. The adjoining histograms show the grain size distributions.

obtained with thick carbon overlayers, (Figures 4.7d and e) exhibit typical interparticular spacings of ~7 and ~19 nm, respectively.   Thus, the presence of an intervening carbon layer seems to provide porous channels for aurate ions to get reduced at the Si surface by electroless means. The

morphology of the resulting Au deposits critically depends on the carbon layer thickness. In another study, the Au deposition was carried out initially for 40 minutes followed by 80 minutes (with a break but for a total of 120 minutes), on a 90 nm thick carbon overlayer, the morphology of the obtained granules was altogether different (compare Figure 4.7d and f). This further illustrates the process of metal reduction in the pores of carbon overlayer.
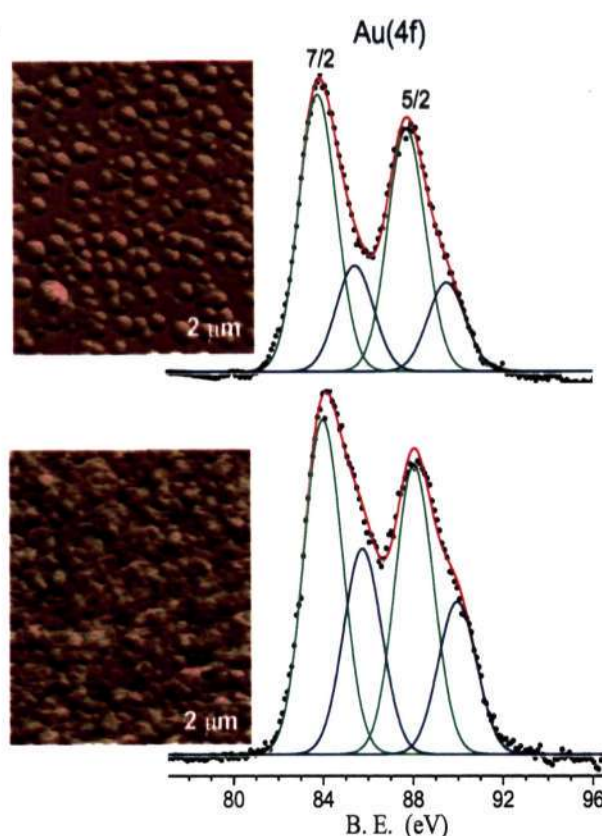
Figure 4.8 AFM images (1 x 1 μm^2) showing the morphology of the film (a) before and (b) after annealing at 250 °C for 2 hours. The corresponding core level spectra are also shown.

We have also examined the affect of annealing on the morphology and the chemical state of Au. For this purpose, a Si substrate with a 90 nm thick carbon overlayer and 60 minutes of Au deposition was subjected to annealing at 250 °C for 2 hours. From the AFM images in Figure 4.8,

we observe that the Au granules appear rounded following annealing. The corresponding 4f core level spectrum shows that the Au^{1+} species is reduced to half of its intensity in the as-prepared substrate. Clearly, annealing induces reduction of Au^{1+} to Au^0 but with some loss of metal due to evaporation. In order to assess the porous nature of the deposits
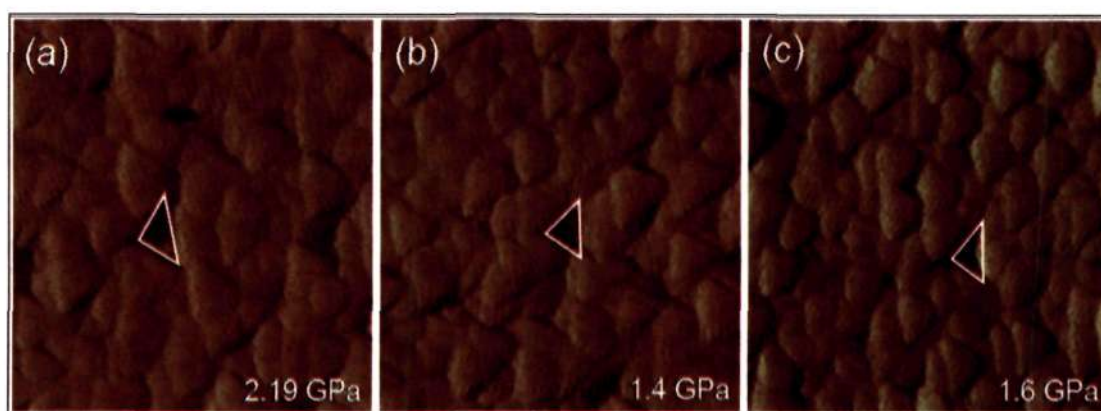
Figure 4.9   Tapping mode image showing the indented films ($1 \times 1\mu m^2$) prepared by 120 minutes of Au deposition over carbon layers of thickness, (a) 0 nm, (b) 12 nm and (c) 90 nm. The white triangles marked indicate the indented region

(carbon and Au), we have made indents using an AFM probe (see Section 2.4) on the substrates with different carbon overlayer thicknesses (Figure 4.9). In all these cases, Au deposition was carried out for 120 minutes. The indented regions are clearly visible as prismatic depressions on the substrates. The estimated hardness for the substrate without a carbon overlayer was 2.19 ± 0.1 GPa, close to the expected for sputtered Au films [66]. Interestingly, the hardness values for the substrates with 15 and 90 nm thick carbon overlayers were much lower - 1.4 ± 0.1 and 1.6 ± 0.1 GPa clearly indicating the soft nature of the carbon and Au deposits.

4.3.3 Summary

In summary, we find that the carbon overlayer thickness on Si substrates increases linearly with respect to the time of laser deposition as measured from profilometry. At higher deposition times, the carbon layer became increasingly amorphous as evident from the relative intensity of the D peak in Raman measurements. In contrast to Au electroless deposition on bare Si substrates, the deposition on the substrates precoated with carbon did not show appreciable increase in the film thickness. However, the metal deposition was found to be significant from the core level spectral measurements. Interestingly, besides Au^0 species a noticeable proportion of Au^{1+} species (Au^{3+} to a small extent) was found with substrates precoated with carbon. This may be due to the formation of a surface gold carbidic species within the pores of the amorphous carbon layer. Annealing the substrates in oxygen atmosphere improved the morphology of the Au deposits besides reducing the proportion of Au^{1+} species.

Although Au deposition did not add to the thickness of the film on Si substrates, an examination of the morphology using AFM did reveal the presence of Au granules. The size and the nature of the packing of the granules critically depend on the underlying carbon film thickness. While substrates with no or less thickness of carbon (15 nm) produce large granules (220-280 nm and 90-110 nm, respectively) that appeared glued to each other, those with more carbon (90 and 190 nm) contained small circular granules (30-60 nm and 40-80 nm) with large intergranular

spacing 7 and 19 nm). The hardness values of the deposits containing both Au and carbon, measured using nanoindentation on an AFM setup, were considerably lower ($\sim$1.15 GPa) compared to Au deposition on bare Si ($\sim$2.19 GPa) - an observation that lends further support to the soft nature of the deposits.

4.4 SERS studies on Au-C/Si substrates

The ability to control the granule size prompted us to examine the possibility of using Au-C/Si substrates for SERS activity. For this purpose, substrates were selected all with Au deposition of 120 minutes. The AFM images of the six substrates are presented in Figure 4.7. It may be recalled that the substrate (a) was prepared with Au deposition on bare Si (with no carbon) while (b), (c), (d) and (e) with carbon layer thickness of 15, 45, 90 and 190 nm respectively. The substrate (f) was prepared under similar conditions as substrate (d) except that the Au deposition process was carried out in two split durations (40 + 80 minutes). We have measured the SERS activity of the substrates in the presence of analyte-nanoparticle mixture. The desired Au sol was prepared following Lee and Meisel method [83]. Accordingly, 240 mg of $HAuCl_4$ was dissolved in 500 mL of water and the solution was brought to boiling. A 50 mL of 1% sodium citrate solution was added to the boiling solution. The boiling continued for $\sim$1 hour and the resulting sol was then cooled. The test molecule, thiophenol (1 mM in ethanol), was added to the sol in the ratio of 1:4 and left for adsorption for 16 hours. The TEM image of Au
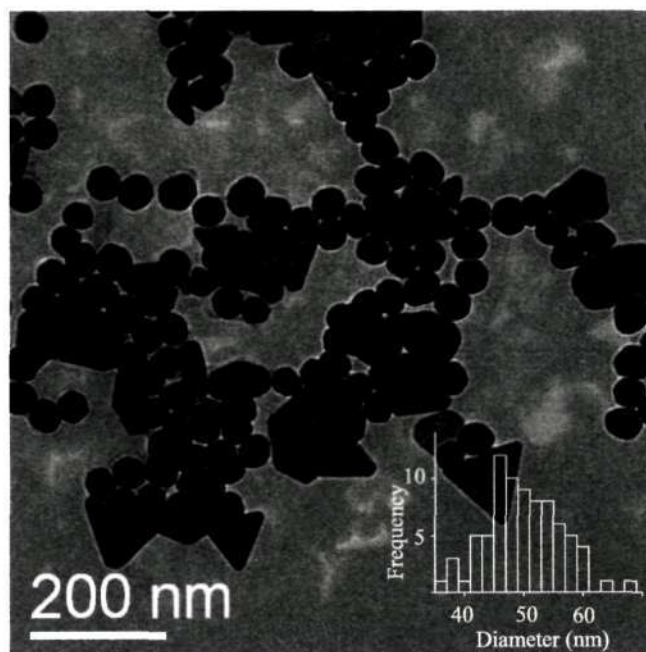
Figure 4.10 TEM image showing the Au colloids formed by citrate reduced method. Histogram showing the particle size distribution is shown in the inset.

colloids is shown in Figure 4.10. We observe a bimodal growth pattern with most of the colloids being spherical in shape and few with plate-like morphology having triangular and hexagonal geometries. The thickness of these non-spherical colloids is less compared to the spherical ones. This is evident from the contrast seen in the TEM image of spherical and non-spherical colloids. The histogram in the inset shows the distribution in size of spherical shaped colloids. They are distributed over the range of 35-70 nm, their mean diameter being ~45 nm. The size of the triangular colloids ranges from 45-110 nm, with mean size being ~75 nm and the thickness ~35 nm.

A 40 μL of the sol carrying thiophenol was drop-coated on the Au substrates and left for overnight drying at room temperature. For SERS

measurements, a 632 nm He-Ne Laser coupled to a custom built Raman microscope was used. SERS spectra were recorded in range 900-1200 cm^{-1}. A holographic grating (1800 grooves mm^{-1}) in combination with a 500 μm entrance slit provided a resolution of $\sim$4 cm^{-1}. The laser power at the sample was 5 mW. We chose thiophenol as a test molecule for SERS
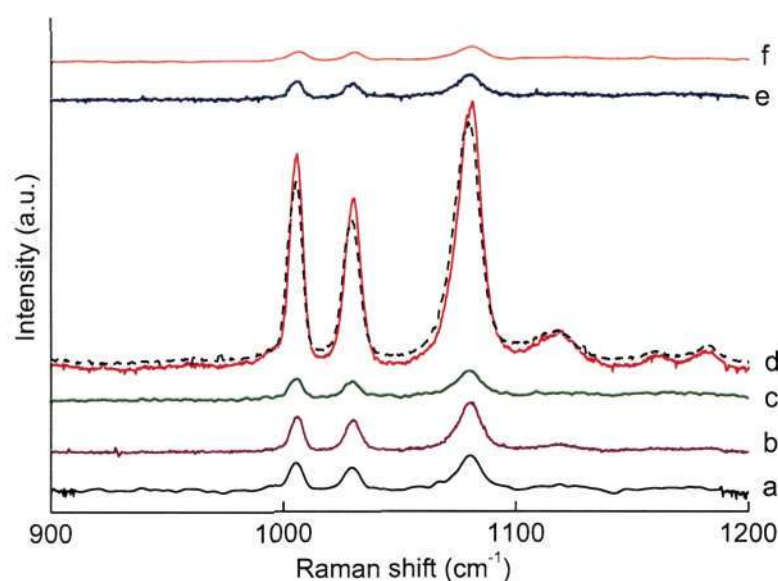
Figure 4.11   SERS spectra of thiophenol on substrates (a), (b), (c), (d), (e) and (f). The spectra are vertically shifted for clarity. The dashed line indicates the reusability of the substrate (d).

measurements since its adsorption has been well studied thoroughly on Au surface. Figure 4.11 shows the SERS spectra of thiophenol in the range of 900-1200 cm^{-1} from the six substrates.The band assignments for the thiophenol molecule is given in Table 4.1. The spectral intensity was similar from different regions on a given substrate, something characteristic of the substrate itself. The intensity is found to be similar in the case of substrates (a), (b) and (d) while we see an order of magnitude

Table 4.1 Surface enhanced Raman Scattering band assignments

Molecule	Raman shift (cm^{-1})	SERS band assignment
Thiophenol	1005	C-H ring
	1030	C-H bending
	1081	C-S stretching
Rodamine 6G	622	C-C-C stretching
	773	C-H out of plane bending
	1126	C-H in plane bending
	1186	C-C stretch
	1367	aromatic C-C stretch
	1513	aromatic C-C stretch
	1580	aromatic C-C stretch
ATP	737	Ring breathing
	1034	Ribose vibration
	1325	C-N stretching
	1473	C=N stretching
Adenine	740	ring breathing mode
	1265	ring-CH$_3$ stretching
	1372	C-N stretching (Pyridine)
	1455	C=N stretching (Pyridine)

increase for substrate (d). It is interesting to note that the intensity of these modes in substrate (e) is similar to that on substrate a, b or c. Following the procedure described by Zhu et al.[105], the enhancement factors were estimated to be 0.33 x 10^6, 0.46 x 10^6, 0.44 x 10^6, 2.67 x 10^6 and 0.34 x 10^6 for substrates (a), (b), (c), (d) and (e) respectively. It has been reported that SERS is most effective when the size of the nanoparticles is in the range of ~50 nm [102], which is the case with

the substrate (d) (see Figure 4.7d). There could be an additional reason for this observation. It is known that the Raman signal is sensitive to the arrangement of nanoparticles in a given aggregate [106,107]. Here in this case, the size of the nanoparticles added atop is similar to the size of the granules of substrate (d), and therefore, we expect increased plasmon resonance coupling and electromagnetic field enhancement. In the case of substrate e, even though the granule size is comparable, the large interparticle separation ($\sim$19 nm) does not permit an effective coupling. For substrate f, the enhancement factor is estimated to be 0.22×10^6 which is a magnitude lower when compared with substrate d, proving that underlying carbon is playing a crucial role in determining the particle size. An useful aspect of these SERS substrates is that they can be washed and reused. Following a thorough wash in double distilled water, the substrate d was devoid of any spectral intensity and the intensity regained nearly fully after reloading the analyte-nanoparticle system (see dashed curve in Figure 4.11).

Carbon deposition on Si has carried out by other methods as well. Lampblack carbon was deposited Si(100) substrate by placing it over a flame at a distance of 5 cm for 2 minutes. In the arc discharge method, a cleaned Si substrate was placed 10 cm below the graphite electrodes a vacuum chamber (10^{-7} torr) and a current of 50 A was applied across the electrodes, to strike an arc. Following carbon deposition, Au was deposited in the usual way for 120 minutes in the standard plating solution and the substrate was washed with double distilled water and
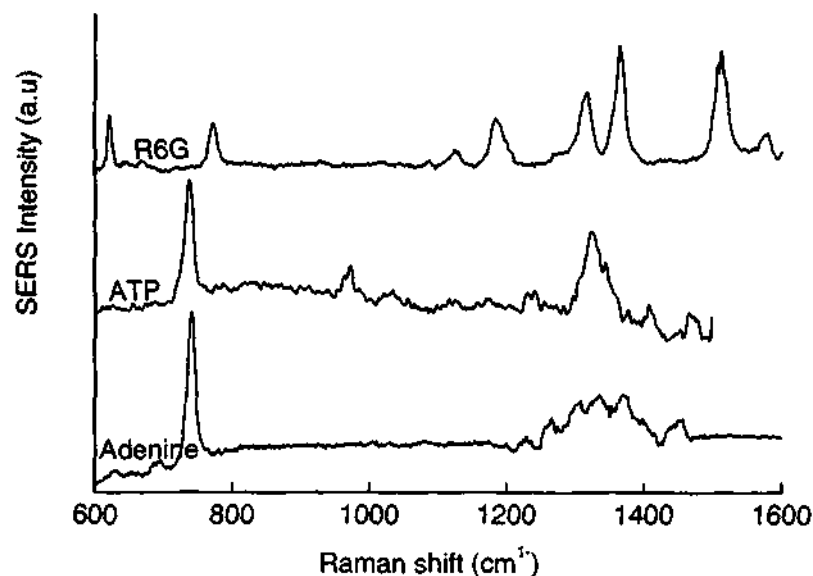
Figure 4.12 SERS spectra of rodamine 6G (R6G) dye, adenosine triphosphate (ATP) and adenine.

dried under flowing argon. The carbon overlayer thickness was found to be 360 nm. SERS measurements done on this substrate showed an enhancement factor of 0.45×10^6, comparable to substrate (e).

We have tried our substrates (d) for rodamine 6G (R6G) as well as for biomolecules such as adenosine triphosphate (ATP) and adenine using the procedure adopted for thiophenol. The spectral features are clearly evident [85,87,90] as shown in Figure 4.12. The band assignments for the molecules is given Table 4.1.

In Figure 4.13, we show a plot of concentration versus Raman intensity to determine the detection limit for R6G molecule. The concentration of R6G in the analyte-nanoparticle system has been varied and we were able to detect R6G with a concentration as low as 5×10^{-10} M. Taking into account the volume probed by the laser during this measurement to

be 10 μm x 10 μm x 100 μm [84], it is estimated that 3 or 4 molecules may reside within the probe region. Thus, the substrates produced can be used for ultrasensitive detection of molecules. We have also tested the ability of the substrates for functionalization. For this purpose, substrate (d) was dipped for 2 hours in an ethanolic solution of 1,8-dithiol [108]. It is noteworthy that the substrate produced a spectrum comparable to curve d in Figure 4.11.
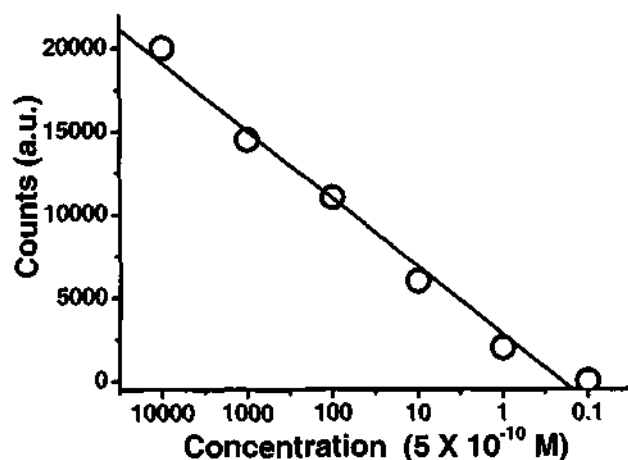
Figure 4.13   A plot of concentration versus the intensity of R6G detected.

In summary, a new method of producing SERS substrates consisting of nanogranular gold on carbon, deposited sequentially on Si(100) surfaces has been developed. The molecules of interest, thiophenol, R6G, ATP and adenine were carried to the substrates on citrate reduced Au nanoparticles. By varying the carbon layer thickness prior to Au deposition, we have been able to arrive at an optimal size for the Au nanogranules on the substrate and thus a maximum Raman signal enhancement factor of 3 x 10^6. With such sensitivity, the lowest

concentration of the molecules detectable was 5 x 10^{-10} M which considering the probe volume, translates to nearly single molecule detection. Importantly, SERS substrates can be washed, reused as well as be functionalized.

Bibliography

[1] Special issue on Nanostructured Materials, Chem. Mater. **1996**, *8*.

[2] Special issue on Nanoscale Materials, Acc. Chem. Res. **1999**, *32*.

[3] M. Faraday, Philos. Trans. R. Soc. London. **1857**, *147*, 145.

[4] Y. Xia, P. Yang, Y. Sun, Y. Wu, B. Mayers, B. Gates, Y. Yin, F. Kim, H. Yan, Adv. Mater. **2003**, *15*, 353.

[5] J. Aruna, B. R. Mehta, L. K. Malhotra, S. A. Khan, D. K. Avasthi, J. Nanosci. Nanotechnol. **2005**, *5*, 1728.

[6] F. Jiménez-Villacorta, A. Muñoz-Martín, M. Vila, C. Prieto, A. Traverse, Phys. Scipta *(in press)*.

[7] D. Babonneau, A. Naudon, T. Cabioc'h, O.Lyon, J. Appl. Cryst. **2000**, *33*, 437.

[8] D. Perednis, L. J. Gauckler, J. Electroceramics **2005**, *14*, 103.

[9] A. Watanabe, M. Unno, F. Hojo, T. Miwa, Mater. Lett. **2003**, *57*, 3043.

[10] S. C. Glade, T. W. Trelenberg, J. G. Tobin, A. V. Hanza, Mat. Res. Soc. Symp. Proc. **2004**, *804*, DD5.5.1.

[11] P. John Thomas, G. U. Kulkarni, C. N. R. Rao, J. Nanosci. and Nanotechnol. **2001**, *1*, 267.

[12] N. O'Shea, M. A. Phillips, M. D. R. Taylor, P. Moriarty, M. Brust, V. R. Dhanak, Appl. Phys. Lett. **2002**, *81*, 5039.

[13] V. V. Agarwal, G. U. Kulkarni, C. N. R. Rao, J. Phys. Chem. B **2005**, *109*, 7300.

[14] G. McMohan, U. Erb, J. Mater. Sci. Lett. **1989**, *8*, 865.

[15] G. Oskam, J.G. Long, A. Natarajan, P.C. Searson, J. Phys. D: Appl. Phys. **1998**, *231*, 1927.

[16] N. V. Parthasardhy, Practical Electroplating Handbook, Prentice Hall, Englewood Cliffs, NJ, **1989**.

[17] M. L. Munford, F. Maroun, R. Cortès, P. Allongue, A. A. Pasa, Surf. Sci. **2000**, *537*, 95.

[18] R. Würschum, S. Gruss, B. Gissibl, H. Natter, R. Hempelmann, H. E. Schäfer, Nanostr. Mater. **1997**, *9*, 615.

[19] A. P. O'Keeffe, O. I. Kasyutich, W. Schwarzacher, L. S. de Olivera, A. A. Pasa, Appl. Phys. Lett. **1998**, *73*, 1002.

[20] K. Attenborough, H. Boeve, J. De Boeck, G. Borghs, J. P. Celis, Appl. Phys. Lett. **1999**, *74*, 2206.

[21] B. J. Hwang, R. Santhanam, Y. L. Lin, J. Electrochem. Soc. **2000**, *417*, 2252.

[22] B. J. Hwang, R. Santhanam, Y. L. Lin, Electroanalysis **2003**, *15*, 1667.

[23] G. Palumbo, J. L. McCrea, U. Erb, Encyclopedia of Nanoscience and Nanotechnology, *1*, 89.

[24] J. C. Ziegler, G. Scherb, O. Bunk, A. Kazimirov, L. X. Cao, D. M. Kolb, R. L. Johnson, J. Zegenhagen, Surf. Sci. **2000**, *452*, 150.

[25] F. Ronkel, J. W. Schultze, R. Arens-Fischer, Thin Solid Films **1996**, *276*, 40.

[26] H. Morinaga, M. Suyama, T. Ohmi, J. Electrochem. Soc. **1994**, *141*, 2834.

[27] L. Magagnin, R. Maboudin, C. Carraro, Electrochem. Solid State Lett. **2001**, 4, C5.

[28] L. Magagnin, R. Maboudian, C. Carraro, Thin Solid Films **2003**, *434*, 100.

[29] T. Homma, C. P. Wade, C. E. D. Chidsey, J. Phys. Chem. **1998**, *41*, 7919.

[30] G. J. Norga, M. Platero, K. A. Black, A. J. Reddy, J. Michel, L. C. Kimerling, J. Electrochem. Soc. **1997**, *144*, 2801.

[31] J. Shu, B. P. A. Grandjean, S. Kaliaguine Ind. Eng. Chem. Res. **1997**, *36*, 1632.

[32] L. A. Nagahara, T. Ohmori, K. Hashimoto, A. Fujishima, J. Vac. Sci. Technol. A **1993**, *11*, 763.

[33] C. H. Ting, M. Paunovic, J. Electrochem. Soc. **1989**, *136*, 486.

[34] P. Gorostiza, M. Kulandainathan, R. Diaz, F. Sanz, P. Allongue, J. R. Morantes, J. Electrochem. Soc. **2000**, *147*, 1026

[35] S. Furukawa, M. Mehregany, Sensors Actuators A **1996**, *56*, 261.

[36] V. L. Liang, R. Chen, O. Chyan, Am. Jol. Undegrad. Res. **2002**, *1*, 1.

[37] G. V. Kuznetsov, V. A. Skryshevsky, T. A. Vdovenkova, A. I. Tsyganova, P. Gorostiza, F. Sanz, J. Electrochem. Soc. **2001**, *148*, C528.

[38] P. Gorostiza, R. Diaz, J. Servat, F. Sanz, J. R. Morante, J. Electrochem. Soc. **1997**, *144*, 909.

[39] P. Gorostiza, J. Servat, J. R Morante, F. Sanz, Thin Solid Films **1996**, *275*, 12.

[40] Y. Sacham-Diamond, A. Inberg, Y. Sverdlov, N. Croitoru, J. Electrochem. Soc. **2000**, *147*, 3345.

[41] A. K. Kalkan, S. J. Fonash, J. Phys. Chem. B **2005**, *109*, 20779.

[42] I. B. Krikshtopaitia, Z. P. Kudzhmauskaite, Elektrokhimiya **1971**, 7, 1679.

[43] L. Magagnin, R. Maboudian, C. Carraro, J. Phys. Chem. B **2002**, *106*, 401.

[44] S. Warren, A. Reitzle, A. Kazimirov, J. C. Ziegler, O. Bunk, L. X. Cao, F. U. Renner, D. M. Kolb, M. J. Bedzyk, J. Zegenhagen, Surf. Sci. **2002**, *496*, 287.

[45] C. Rossiter, I. I. Suni, Surf. Sci. **1999**, *430*, L553.

[46] L. A. D'Asaro, S. Nakahara, Y. Okinaka, J. Electrochem. Soc. **1980**, *127*, 1935.

[47] E. Delamarche, J. Vichiconti, S. A. Hall, M. Geissler, W. Graham, B. Michel, R. Nunes, Langmuir, **2003**, *19*, 6568.

[48] P. C. Hidber, W. Helbig, E. Kim, G. M. Whitesides, Langmuir **1996**, *12*, 1375-1380.

[49] P. C. Hidber, P. F. Nealey, W. Helbig, G. M. Whitesides, Langmuir **1996**, *12*, 5209.

[50] Y. Xia, N. Venkateswaran, D. Qin, J. Tien, G. M. Whitesides, Langmuir **1998**, *14*, 363.

[51] S-H. Zhang, Z-X. Xie, Z-Y. Jiang, R-B. Huang, L-S. Zheng, Chem. Comm. **2004**, 1106.

[52] N. Tokuda , N. Sasaki, H. Watanabe, K. Miki, S. Yamasaki, R. Hasunuma, K. Yamabe, J. Phys. Chem. B **2005**, *109*, 12655.

[53] R. W. Zehner, L. R. Sita, Langmuir **1999**, *15*, 6139.

[54] A. Carvalho, M. Geissler, H. Schmid, B. Miche, E. Delamarche Langmuir **2002**, *18*, 2406.

[55] J. Li, M. Moskovits, T. L. Haslett, Chem. Mater. **1998**, *10*, 1963.

[56] L.-M. Ang, T. S. A. Hor, G.-Q. Xu, C.-H. Tung, S. Zhao, J. L. S. Wang, Chem. Mater. **1999**, *11*, 2115.

[57] A. M. Bittner, M. Knez, S. Balci, A. Kadri, C. Wege, H. Jeske, K. Kern, European Cells and Mater. **2003**, *6*, 80.

[58] M. E. Gertner, M. Schlesinger, Electrochem. and Solid-State Lett. **2003**, *6*, J4.

[59] P. Jacob, Y. J. Chabal, J. Chem. Phys. **1991**, *95*, 2897.

[60] K. Oura, V. G. lifshits, A. A. Saranin, A. V. Zotov, M. Katayama, Surf. Sci. Report **1999**, *35*, 1.

[61] Y. Kuwahara, S. Natatani, M. Takahasi, M. Aono, T. Takahashi, Surf. Sci. **1994**, *310*, 226.

[62] N. Mancini, E. Rimini, Surf. Sci. **1970**, *22*, 357.

[63] N. G. Semaltianos, E. G. Wilson, Thin Solid Films **2000**, *366*, 11.

[64] P. Tangyunyong, R. C. Thomas, J. E. Houston, T. A. Michalske, R. M. Crooks, A. J. Howard, Phys. Rev. Lett. **1993**, *71*, 3319.

[65] M. Salmeron, A. Folch, G. Neubauer, M. Tomitori, D. F. Ogletree, W. Kolbe, Langmuir **1992**, *8*, 2832.

[66] L. Šiller, N. Peltekis, S. Krishnamurthy, Y. Chao, App. Phys. Lett. **2005**, *86*, 221912.

[67] J. C. Arnault, A. Mosser, M. Zamfirescu, H. Pelletier, J. Mater. Res. **2002**, *17*, 58.

[68] A. Rota, A. Martinez-Gil, G. Agnus, E. Moyen, T. Marroutian, B. Bartenlian, R. Mégy, M. Hanbücken, P. Beauvillain, Surf. Sci. **(2006)** *(in press)*.

[69] L. Magagnin, V. Bertani, P. L. Cavallotti, R. Maboudian, C. Carraro, Microelectron. Eng. **2002**, *64*, 479.

[70] H. Kind, M. Geissler, H. Schmid, B. Michel, K. Kern, E. Delamarche, Langmuir **2000**, *16*, 6367.

[71] F. Guan, M. Chen, W. Yang, J. Wang, S. Yong, Q. Xue, Appl. Surf. Sci. **2005**, *240*, 24.

[72] H. Kind, M. Geisser, H. Schmid, B. Michel, K. Kern, E. Delamarche, Langmuir **2000**, *16*, 6367.

[73] A. Kumar, G. M. Whitesides, Appl. Phys. Lett. **1993**, *63*, 2002.

[74] M. Wirtz, C. R. Martin, Adv. Mater. **2003**, *15*, 445.

[75] H. Tsunoyama, H.Sakurai, N. Ichikuni, Y. Negishi, T. Tsukuda, Langmuir **2004**, *20*, 112936.

[76] J. Sagiv, J. Am. Chem. Soc. **1980**, *102*, 92.

[77] R. Maoz, J. Sagiv, J. Colloid Interface Sci. **1984**, *100*, 465.

[78] P. Moriarty, M. D. R. Taylor, M. Brust, Phys. Rev. Lett. **2002**, *89*, 248303.

[79] M. D. R. Taylor, P. Moriarty, and M. Brust, Chem. Phys. Lett. **2001**, 348.

[80] G. A. Baker, D. S. Moore, Anal. Bioanal. Chem. **2005**, *382*, 1751.

[81] M. Moskovits, Rev. Mod. Phys. **1985**, *57*, 783.

[82] A. Campion, P. Kambhampati, Chem. Soc. Rev. **1998**, *27*, 241.

[83] P. C. Lee, D. Meisel, J. Phys. Chem. **1982**, *86*, 3391.

[84] K. L. Norrod, L. M. Sudnik, D. Rousell, K. L. Rowlen, Appl. Spec. **1997**, *51*, 994.

[85] K. Kneipp, H. Kneipp, I. Itzkan, R. R. Dasari, M. S. Feld, J. Phys.: Condens. Matter **2002**, *14*, R597.

[86] J. A. Dieringer, A. D. McFarland, N. C. Shah, Douglas A. Stuart, A. V. Whitney, C. R. Yonzon, M. A. Young, X. Zhang, R. P. V. Duyne, Faraday Discuss. **2005**, *132*, 1.

[87] S. Chan, S. Kwon, T.-W. Koo, L. P. Lee, A. A. Berlin, Adv. Mater. **2003**, *15*, 1595.

[88] M. E. Abdelsalam, P. N. Bartlett, J. J. Baumberg, S. Cintra, T. A. Kelf, A. E. Rusell, Electrochem. Commun. **2005**, *7*, 740.

[89] J. B. Jackson, N. J. Halas, PNAS **2004**, *101*, 17930.

[90] A. M. Schwartzberg, C. D. Grant, A. Wolcott, C. E. Talley, T. R. Huser, R. Bogomolni, J. Z. Zhang, J. Phys. Chem. B **2004**, *108*, 19191.

[91] N. Terasaki, K. Otsuka, T. Akiyama, S. Yamada, Jpn. J. Appl. Phys. **2004**, *43*, 2372.

[92] T. Akiyama, K. Inoue, Y. Kuwahara, Y. Niidome, N. Terasaki, S. Nitahara, S. Yamada, Langmuir **2005**, *21*, 793.

[93] B. Nikoobakht, M. A. El-Sayed, J. Phys. Chem. A **2003**, *107*, 3372.

[94] A. N. Shipway, M. Lahav, R. Gabai, I. Willner, Langmuir **2000**, *16*, 8789.

[95] M. Suzuki, Y. Kuwahara, N. Terasaki, K. Inoue, S. Yamada, J. Phys. Chem. B **2004**, *108*, 11660.

[96] N. Félidj, S. L. Truong, J. Aubard, G. Lévi, J. R. Krenn, A. Hohenau, A. Leitner, F. R. Aussenegg, J. Chem. Phys. **2004**, *120*, 7141.

[97] P. F. Liao, M. B. Stern, Opt. Lett. **1982**, *7*, 483.

[98] L. A. Dick, A. D. McFarland, C. L. Haynes, R. P. V. Duyne J. Phys. Chem. B **2002**, *106*, 853.

[99] A. Wei, B. Kim, B. Sadtler, S. L. Tripp, ChemPhysChem **2001**, *12*, 743.

[100] T. R. Jensen, M. L. Kelly, A. A. Lazarides, G. C.Schsatz, R. P. V. Duyne, J. Phys. Chem. B **1999**, *103*, 9846.

[101] N. Félidj, J. Aubard, G. Lévi, J. R. Krenn, A. Hohenau, G. Schider, A. Leitner, F. R. Aussenegg, Appl. Phys. Lett. **2003**, *82*, 3095.

[102] R. K. Chang, T. E. Furtak, Ed., Surface Enhanced Raman Scattering, Plenum Press.

[103] J. Robertson, Mater. Sci. Eng. R **2002**, *37*, 129.

[104] J. Filik, Raman Spectroscopy **2005**, *1*, 8.

[105] Z. Zhu, T. Zhu, Z. Liu, Nanotechnology **2004**, *15*, 357.

[106] P. Alivisatos, Nat. Biotech. **2004**, *22*, 47.

[107] J. K. Danials, G. Chumanov, J. Phys. Chem. B **2005**, *109*, 17936.

[108] K. V. Sarathy, P. John Thomas, G. U. Kulkarni, C. N. R. Rao, J. Phys. Chem. B **1999**, *103*, 399.

620.5
ρ06